Modelling of NOx Emissions from Gas Turbine Combustors

Master Thesis

Marlena Maćkowiak

TU Delft, 3ME

Studentnumber: 5387582

Supervisors:

Sikke Klein (TU Delft)
Michael Huth (Siemens Energy)
Jürgen Meisl (Siemens Energy)

October 31, 2022

Abstract

The detrimental influence of nitric oxides (NOx) on humans and the environment has been widely discussed by researchers.
The dominant part of nitic oxides emissions comes from combustion - majority of NOx is being produced by reaction of nitrogen and oxygen at high temperatures.

This thesis project is carried out in cooperation with *Siemens Energy*, one of the gas turbines manufacturers.
The gas turbine combustor design requires extensive work in many fields: in addition to temperature distribution and flow field prediction, modelling of acoustics and emissions is necessary. As NOx are influenced by many variables, detailed sensitivity analyses of design features is required. Since that gas turbine producers are developing their own tools for emissions predictions.

The aim of this study is improvement and assessment of the existing tool used by *Siemens Energy* to predict NOx emissions by simulating the combustor system (both the flow and chemical kinetics).
As NOx emissions depend on the air-fuel mixing quality, the tool is equipped with a Monte Carlo-based turbulent mixing model. The combustor flow is divided into small parts - *particles*, that react and exchange properties between each other according to the Curl's turbulent mixing model.

The tool was improved by adding useful features (such as prescribed unmixedness in the flame front). After that, the *Siemens Energy* axially staged combustor was modelled (with different equivalence ratios, pressure levels and pilot fuel flows). In the end the tool was validated - the simulation results were compared to the experimental ones.

Contents

Abstract i

List of Symbols 5

List of Symbols 6

1 Introduction 7

1.1 NOx Characteristics and Impact . . . 7
1.2 NOx Emission Sources . . . 9
1.3 NOx Emissions' Reduction Methods . . . 9
1.4 Gas Turbines . . . 10
1.5 Thesis Aim . . . 11
1.6 Research Questions . . . 11
1.7 Content of the Thesis . . . 11

2 Theorethical Background 13

2.1 Gas Turbine Combustion . . . 13
2.1.1 Adiabatic Flame Temperature . . . 14
2.2 Premixed vs Diffusion Flames . . . 16
2.3 Turbulent Premixed Combustion . . . 18
2.3.1 Flame Structure . . . 18
2.3.2 Flame Regimes . . . 19
2.4 Turbulent Mixing . . . 21
2.4.1 Gas Turbine Premixer . . . 21
2.4.2 Cross Flow Jet . . . 22
2.5 Chemical Kinetics . . . 23
2.5.1 Rate Coefficients' Dependence on Temperature . . . 24
2.5.2 GRI 3.0 Mechanism . . . 24

2.6 NOx formation mechanisms . . . 25
2.6.1 Thermal NO . . . 25
2.6.2 Prompt NO . . . 26
2.6.3 Nitrous Oxide NO . . . 27
2.6.4 Turanyi's corrections to GRI 3.0 . . . 27
2.6.5 NOx Formation in Gas Turbines . . . 27
2.7 Reactor Network . . . 29
2.7.1 Perfectly Stirred Reactor . . . 29
2.7.2 Plug Flow Reactor . . . 30
2.8 Turbulent Mixing Modelling . . . 33
2.8.1 Unmixedness Definition . . . 33
2.8.2 Monte Carlo Algorithm . . . 34
2.8.3 Modified Curl's Model by Pope . . . 34
2.9 Unmixedness Impact on NOx formation . . . 36
2.10 Probability Density Function Approximations . . . 38
2.10.1 Beta Distribution . . . 38

3 Combustor Model 40
3.1 GeneAC structure . . . 40
3.2 Monte Carlo in GeneAC . . . 41
3.2.1 Mixture Fraction . . . 41
3.2.2 Mixing . . . 42
3.2.3 Prescribed pdf function . . . 44
3.2.4 Reactions . . . 47
3.3 ACE Model . . . 48
3.3.1 Inlets . . . 51
3.3.2 PSR . . . 51
3.3.3 PFR . . . 51
3.4 Sensitivity Analysis . . . 52
3.4.1 Chemical Mechanism Evaluation . . . 52
3.4.2 Design of Experiment . . . 54
3.4.3 Monte Carlo Validation . . . 56

3.4.4 Number of Particles . . . 56
3.5 Parameters Selection . . . 57
3.5.1 PSR residence time . . . 57
3.5.2 PSR mixing time scale . . . 57
3.5.3 PFR mixing time scale . . . 57
3.5.4 Mixture fraction pdf in the inlet . . . 57
3.5.5 Chemical Kinetics Mechanism . . . 58

4 Results and Comparison with Experimental Data 59
4.1 Experimental data . . . 59
4.2 Input data sanity check . . . 60
4.2.1 ACE without X Stage . . . 60
4.2.2 ACE with X stage . . . 61
4.3 Impact of the Test Parameters . . . 62
4.4 Axial Staging Effect . . . 64
4.5 Pressure dependence . . . 65
4.6 NOx source . . . 66
4.7 Mixture Fraction Histogram Evaluation . . . 67
4.7.1 Upstream of the Axial Stage . . . 69
4.7.2 Downstream of the Axial Stage . . . 71

5 Summary 75
5.1 Main Achievements . . . 75
5.1.1 Impact of the Equivalence Ratio . . . 75
5.1.2 Pressure Impact . . . 75
5.1.3 Pilot Fraction Impact . . . 76
5.1.4 Axial Staging . . . 76
5.1.5 NOx Pathway . . . 76
5.1.6 Pdf Evaluation . . . 76
5.2 Proposals . . . 76
5.2.1 Flame CFD Investigation . . . 77
5.2.2 Recirculation . . . 77
5.2.3 Mixing . . . 77

5.2.4 Pilot Modelling 77
5.2.5 Mechanism 77

Bibliography **78**

A Design of Experiment **A-1**

B GeneAC Model **B-1**

List of Figures

1.1 European emissions of SO_2, NO_2 and NH_3 in years 1880–2020; source: Hydrology and Earth System Sciences [34] . . . 8

1.2 The evolution of pollutant emissions in comparison to 1990 in EU. The *initial emissions* of $PM2.5$ and $PM10$ are from the year 2000, of the other pollutants - from 1990; source: European Environment Agency [2] . . . 8

1.3 Share of NOx emissions by sector in Europe (2019); source: European Environment Agency [2] . . . 9

2.1 SGT-300 Siemens Energy gas turbine; source - Siemens Energy offerings website [18]. . . . 14

2.2 Constant-pressure adiabatic flame temperature on h-T coordinates; source [38] . . . 15

2.3 Adiabatic flame temperature at STP; source [28] . . . 15

2.4 Premixed vs. diffusive flames . . . 16

2.5 Schematic drawing of ACE system; source: [26] . . . 18

2.6 Superposition of instantaneous flame fronts acquired at different times (a) and the time averaged flame (b); source: [15] . . . 19

2.7 Borghi-Peters diagram showing the regimes of premixed turbulent combustion. Premixed combustion in gas turbines lays in the marked area; source [30] . . . 20

2.8 Thin reaction zones scheme; source - [38] . . . 21

2.9 Scheme of the gas turbine premixing tube; source [26] . . . 22

2.10 Cross-flow turbulent jets used in mixing modeling . . . 22

2.11 Dimensionless concentration C and dimensionless standard variation $\bar{c'}$ - experimental data; source - Galeazzo [16] . . . 23

2.12 Plot of k_1 vs Temperature . . . 26

2.13 Prompt and postflame NOx . . . 28

2.14 PSR scheme with conservation equations . . . 29

2.15 PFR scheme with infinitesimal control volume Δz . . . 31

2.16 Infinitesimal control volume Δz with fluxes of mass, z-momentum, energy and species . . . 32

2.17 CFD-based probability (sampled over generic flame front) and its Gaussian distribution approximation; source [12] . . . 33

2.18 Modified Curl Model mixing scheme . . . 35

2.19 Measured NOx emissions related to different CFD-based unmixedness parameters and comparison against the modeled emissions; source - Dederichs [12] . . . 37

2.20 Measured NOx emissions at the combustion chamber exit vs. "rms fluctuations in fuel concentration" - basically unmixedness; source - Schlegel [33] . . . 37

2.21 Possible shapes of the beta distribution, source: [13] . . . 38

3.1 Mixture fraction pdf evolution while mixing ($\tau_{mix} = 3ms$) . . . 44

3.2 Inlet element with prescribed mixture fraction pdf (top) and simulating the premixer (bottom). . . . 45

3.3 Histogram shape comparison of GeneAC prescribed pdf and CFD histogram at the end of the premixer. . . . 47

3.4 Change of particle properties depending on the ϕ_p . . . 48

3.5 Combustor position in the Siemens Energy gas turbine; source - Siemens Energy offerings website [18]. . . . 49

3.6 ACE scheme divided into stages: A, B, X and the Pilot. . . . 49

3.7 The division of the cross-sectional area into stages A, B and the Pilot. . 50

3.8 Model of the ACE. The axial dimension is scaled to non-dimensional value x=(0,1). Cross section areas are presented as fractions of the initial area A. 51

3.9 NOx vs. equivalence ratio for different mechanisms at $1bar$, left plot: $\phi \in (0.37, 2.0)$, right plot: zoomed in $\phi \in (0.37, 0.87)$ . . . 53

3.10 NOx vs. equivalence ratio for different mechanisms at $20bar$, left plot: $\phi \in (0.37, 2.0)$, right plot: zoomed in $\phi \in (0.37, 0.87)$ . . . 53

3.11 Pareto chart for the examined parameters . . . 55

3.12 Prescribed pdfs in the mixture inlets . . . 58

4.1 Temperature vs. equivalence ratio dependence for all the test cases. . . . 60

4.2 Scaled NOx vs. equivalence ratio for cases without the X stage (left plots) and with X stage (right plots). Upper plots have $p = 8bar$, for lower ones $p = 16bar$ . . . 63

4.3 Comparison of two exponential curves: with and without axial staging. 64

4.4 $\Delta_{staging}$ vs. ϕ for experiment and simulations. Left plot - $p = 8bar$, right plot - $p = 16bar$. 65

4.5 ξ vs. ϕ for experiment and simulations. On the left combustion without the X stage, on the right with X stage. 66

4.6 Cross sections with extracted mixture fraction histograms. 68

4.7 Legend 69

4.8 Mixture fraction histograms comparison at $x = 0.06$, CFD - red and GeneAC - blue. 70

4.9 Mixture fraction histograms comparison at $x = 0.19$, CFD - red and GeneAC - blue. 70

4.10 Mixture fraction histograms comparison at $x = 0.29$, CFD - red and GeneAC - blue. 71

4.11 Mixture fraction histograms comparison at $x = 0.46$, CFD - red and GeneAC - blue. Left plot: $\tau_{mix,downstream} = 1ms$, right plot: $\tau_{mix,downstream} = 2ms$. 72

4.12 Mixture fraction histograms comparison at $x = 0.57$, CFD - red and GeneAC - blue. Left plot: $\tau_{mix,downstream} = 1ms$, right plot: $\tau_{mix,downstream} = 2ms$. 72

4.13 Mixture fraction histograms comparison at $x = 0.68$, CFD - red and GeneAC - blue. Left plot: $\tau_{mix,downstream} = 1ms$, right plot: $\tau_{mix,downstream} = 2ms$. 73

4.14 Mixture fraction histograms comparison at $x = 0.78$, CFD - red and GeneAC - blue. Left plot: $\tau_{mix,downstream} = 1ms$, right plot: $\tau_{mix,downstream} = 2ms$. 73

4.15 Unmixedness vs. axial position for the CFD data, GeneAC with $\tau_{mix,downstream} = 1ms$ and GeneAC with $\tau_{mix,downstream} = 2ms$ 74

B.1 Legend for the models presented in the Fig. B.2 . . . . . B-1

B.2 The model of combustor used in GeneAC (with axial stage X included - on the left side and without including the X stage: on the right side). . . B-2

List of Tables

2.1 Main characteristics of the beta distribution 39

3.1 Example of an ignition cloud 48
3.2 Parameters of the sensitivity analysis 54
3.3 Monte Carlo Tool Validation 56
3.4 Number of particles impact on NOx (dry, 15%O_2) 56

4.1 Altered parameters of the experiments 59
4.2 Results for the non-X-stage cases 61
4.3 Results for the X-stage cases 61
4.4 Reactions deactivated in each altered mechanism 67
4.5 Different NOx pathway contributions 67

A.1 Sensitivity analysis results A-2

List of Symbols

ϕ	equivalence ratio [−]
R	universal gas constant $8.314 \frac{J}{K \cdot mol}$
T	temperature $[K]$
p	pressure $[Pa]$
U	unmixedness [%]
τ_{mix}	turbulent mixing time scale $[ms]$
τ_{res}	residence time $[ms]$
m_p	particle mass $[kg]$
H_p	particle enthalpy $[J]$
f_p	particle mixture fraction [−]
$\overrightarrow{y_p}$	vector of particle mass fractions [-]
PMP	pilot fraction [−]
$\Delta_{staging}$	reduction in NOx emissions due to axial staging [%]
ξ	pressure dependence power [−]

List of Abbreviations

CFD	Computational Fluid Dynamics
PSR	Perfectly Stirred Reactor
PFR	Plug Flow Reactor
ACE	Advanced Combustion System for high Efficiency

Chapter 1

Introduction

1.1 NOx Characteristics and Impact

Industrial revolution has changed not only the social and political situation in Europe. In the last centuries Europe (as well as the rest of the world) has undergone a large degradation of air quality. As most of the industry was dependent on combustion of fossil fuels, the exhaust gases and dust concentrations have risen significantly (especially in densely populated urban areas).

One of the anthropogenic pollutants widely produced by the industry is NOx. It is a collective name of nitric oxides: NO and NO_2. Their detrimental influence on the environment has been widely discussed by researchers. NOx are the major cause of photo-chemical smog [35]. Urban air ozone (O_3), also formed by photo-chemical decomposition of NO_2 reduces lung functionality and may cause lung inflammation ([39] and [3]).
Additionally, together with SOx, NO_2 reacts with atmospheric water causing acid rains. These rains induce peril to freshwater ecosystems, crops and forests [37].

The historical track of NO_2 and SO_2 anthropogenic emissions is presented in Fig. 1.1.

It was just late twentieth century, when countries in our continent took action in stopping the pollution (visible in the drop of emissions after 1990 in Fig. 1.1). The governments of European Union started to gradually lower the pollution ceilings by forcing the member states' industries to limit their NOx emissions. An example of European NOx reducing policy is the set of *Emission Standards Euro 1 - 6* - directives limiting pollutants in road transport by setting the limits for each type of machines (passenger cars, trucks or motorcycles). The decrease in anthropological emissions is presented in detail in Fig. 1.2. This plot shows a sharp, satisfying SOx reduction (green line), whereas NOx emissions are still at around 30% of the production in 1990 (violet line). Further nitric oxides cutting is one of the goals set for the European industry nowadays.

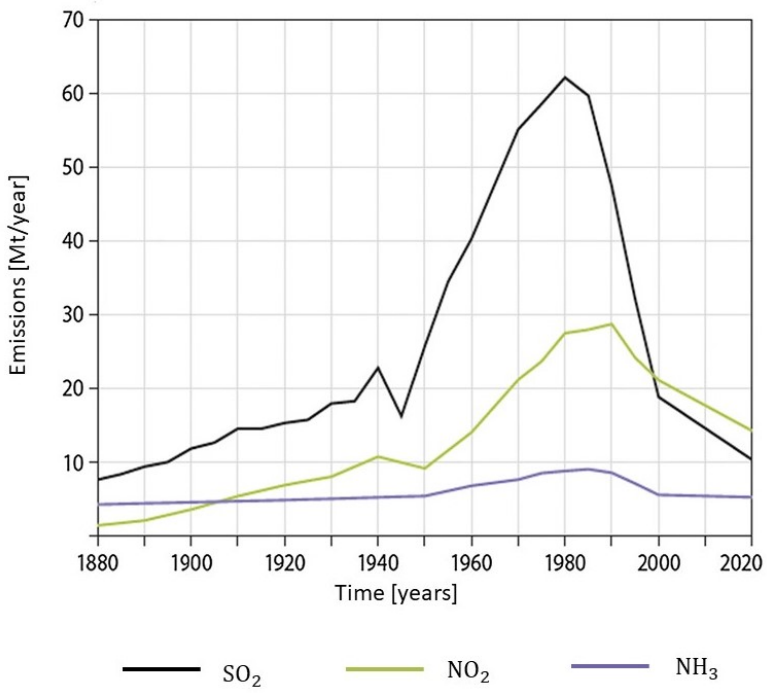

Figure 1.1: European emissions of SO_2, NO_2 and NH_3 in years 1880–2020; source: Hydrology and Earth System Sciences [34]

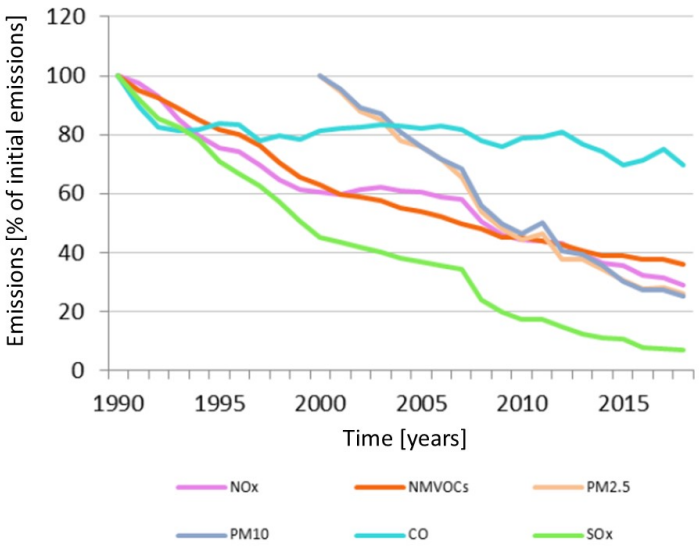

Figure 1.2: The evolution of pollutant emissions in comparison to 1990 in EU. The *initial emissions* of $PM2.5$ and $PM10$ are from the year 2000, of the other pollutants - from 1990; source: European Environment Agency [2]

1.2 NOx Emission Sources

The sources of anthropogenic NOx emissions are presented in the chart 1.3. The largest shares of NOx pie come from road transport and energy industry, so the technology branches requiring combustion. It is because the vast majority of NOx is being produced by reaction of nitrogen (coming from fuel or air) and oxygen (in air) at high temperatures. The combustion associated NOx formation mechanisms are extensively described in Section 2.6.

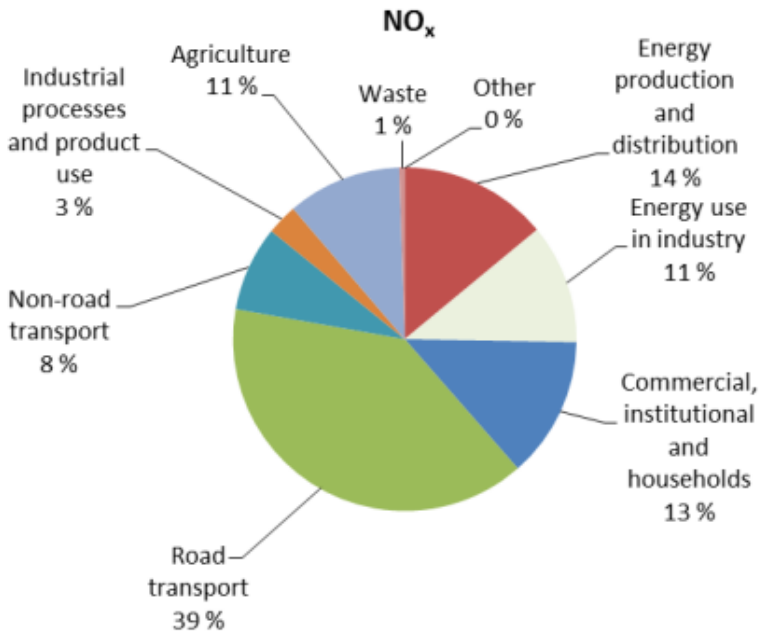

Figure 1.3: Share of NOx emissions by sector in Europe (2019); source: European Environment Agency [2]

As shown in the plot, an important source of non-combustion NOx is also agriculture. Plants produce NOx naturally in microbial processes, but those emitted amounts are limited by environmental conditions such as inorganic nitrogen availability or soil temperature. Agricultural practices like fertilization and irrigation change the environmental variables and increase the NOx emissions dramatically [22].

1.3 NOx Emissions' Reduction Methods

In the last decades, standard measures for NOx reduction have been developed. The basic classification divides them into *primary* and *secondary measures*. Primary ones require

modifications of combustion processes, so are applicable only for the new combustion systems. In contrary, secondary methods are applied in the post-combustion processes (e.g. in the exhaust), so changes in the combustor itself are not necessary.

The idea behind most primary measures is lowering the maximal temperature in the combustor. It can happen by means of dilution with an inert gas such as nitrogen, water or exhaust gases, that takes some of the combustor heat with its heat capacity.
Another NOx reduction technique is lean-premixed combustion, that has become a state-of-art technology in last decades (described in detail in 2.3). Premixing the air-fuel mixture before ignition unifies the temperature in the combustor (to avoid hot spots). As NOx production is intensified in high temperatures, the premixing quality (umixedness reduction) is an issue of particular importance in the NOx production.
Other primary measures are: minimizing the residence time in the combustor (while ensuring all the fuel burned) to limit the exposure of the mixture to the hot temperature conditions and catalytic combustion [40].

A well known post-combustion measure is the catalytic converter placed commonly in the cars' exhaust systems [23]. In this device combination of noble metals oxidize CO to CO_2 and NO to N_2.
In case of stationary power plants, ammonia accompanied catalyst that reacts with NO to produce N_2 and H_2O is being applied. This solution is called the *selective catalytic reduction (SCR)*, that works in a wide range of temperatures, but is prone to fouling of sulfur and particulates in the exhaust [7].
Another popular secondary approach is the *selective non-catalytic reduction* of NO *(thermal DeNOx)*. In this method ammonia flow is added to the exhaust stream and at high temperatures reacts with OH to form NH_2. Then NH_2 reacts with NO and forms water and N_2 (or N_2H, which leads to N_2 as well) [7].

1.4 Gas Turbines

Natural gas combustion was responsible for the production of 16% of electricity in EU in 2013 [32]. Even tough energy technology is striving towards renewable sources, gas turbines are and will remain very important in the energy market. As renewables are characterized by non-uniform production (dependence on weather conditions such as wind, sunlight intensity) additional conventional energy source is necessary for reliable supply. As gas turbines are powered by combustion, they generate NOx. Especially, since producers and clients are aiming at high efficiency, temperature in the combustors has risen much in the last decades (high temperatures favour NOx formation - see 2.6).

1.5 Thesis Aim

The European industry has made large progress in the NOx limitations in the last couple of decades. At the same time, there is still a lot of space for improvements. This thesis project is planned to contribute to the NOx emissions' reduction. Carried out under the aegis of Siemens Energy, "Modelling of NOx Emissions from Gas Turbine Combustors" is a result of cooperation with one of the power industry leaders. Using both company's and university's tools and resources, this thesis project will contribute to limiting the NOx emissions.

The gas turbine combustor design is a very costly task. It requires extensive work in many fields: in addition to temperature distribution and flow field prediction, modelling of acoustics and emissions is necessary. As the industry is striving for simultaneously high efficiency and low emissions, the truly optimal solutions have to be found. The most accurate way of comparing combustor models would be by means of experiments. Unfortunately building and testing each combustor arrangement would require excessive amount of time and money. Even CFD (Computational Fluid Dynamics) simulations are not computationally efficient, especially not applicable to resolve nuances of NOx emissions under multiple different parameter combinations [12]. As NOx are influenced by many variables, detailed sensitivity analyses of design features is required. Since that gas turbine producers are developing their own tools for emissions predictions.

The aim of this study is an improvement and an assesment of the existing tool used by Siemens Energy in examining the NOx emissions on the early design stage of the combustor.

1.6 Research Questions

The tasks of the following thesis project were:

- Overview of a 1D Siemens Energy NOx prediction tool with detailed description,
- Validation of the mentioned prediction tool (including gap analysis),
- Improvement of the existing Monte Carlo codes (used to model unmixedness impact on NOx) based on gap analysis and documenting,
- Checking if they are applicable in Siemens Energy staged combustor system (namely ACE- Advanced Combustion system for high Efficiency).

1.7 Content of the Thesis

After a brief introduction (Chapter 1), the next chapter is describing the theoretical background (Chapter 2). It is where all necessary concepts and phenomena are explained.

In Chapter 3 one can find descriptions of the tool, created models, set parameters and their sensitivity analyses.
The simulation results and their comparison with experiments are found in Chapter 4. Finally, the thesis is summarised in Chapter 5.

Chapter 2

Theorethical Background

2.1 Gas Turbine Combustion

The idea behind any heat machine is the conversion from chemical energy in fuel to heat or useful mechanical energy (that can be further changed into electrical one). Mentioned conversion happens by means of combustion.
By definition combustion is a fast oxidation accompanied with an extensive heat generation. The three basic conditions necessary for burning to occur are: presence of fuel, oxidizer and an ignition source.

In case of gas turbines, pressurized air oxidizes fuel and the products enter the turbine, where they transfer their energy to the shaft. The oxidation takes place in the combustor.

The combustor is a crucial element of all gas turbines. Placed between the compressor and the turbine, ignites the mixture and directs the flow to the turbine.
Tubular (*can*) combustor is consisting of several cylindrical liners mounted on the circular plan. Especially used in early and heavy duty turbines - can combustors need less time and money for their development. Large dimensions and mass are factors limiting its usage in aircraft engines. The Fig. 2.1 shows the SGT-300 Siemens Energy industrial gas turbine (equipped with can combustors).

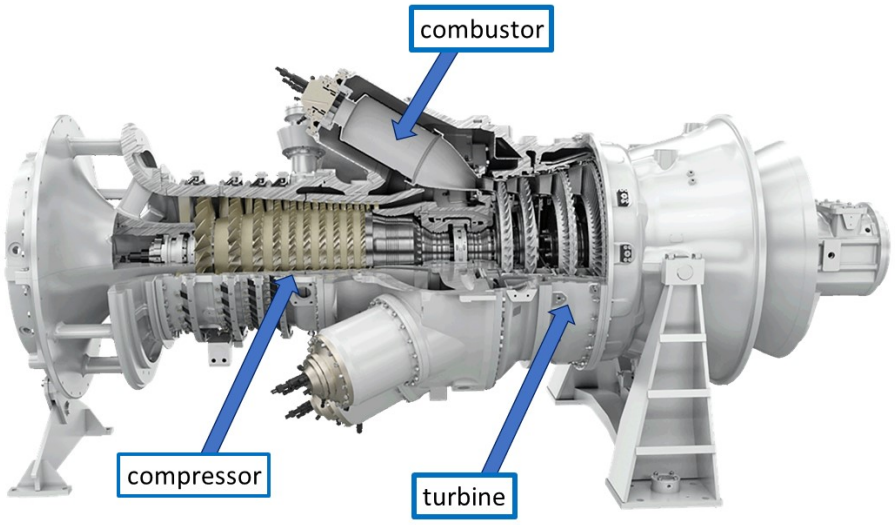

Figure 2.1: SGT-300 Siemens Energy gas turbine; source - Siemens Energy offerings website [18].

Among the others, main requirements for combustors are: high combustion efficiency, small pressure loss, infallible ignition, low emissions and flame stability throughout wide ranges of pressure.

2.1.1 Adiabatic Flame Temperature

In case of adiabatic combustion at constant pressure the specific enthalpy of reactants (at pressure P and temperature T_i) equals the final stage specific products' enthalpy (at P and T_{ad}) - see Fig. 2.2.

$$h_{reac}(T_i, P) - h_{prod}(T_{ad}, P) = 0 \tag{2.1}$$

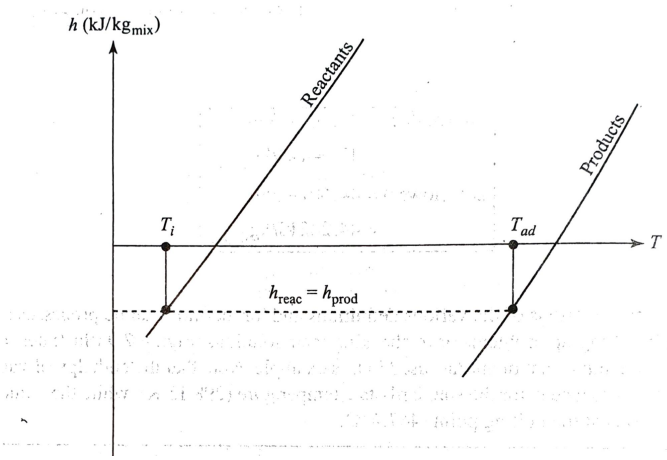

Figure 2.2: Constant-pressure adiabatic flame temperature on h-T coordinates; source [38]

The T_{ad} is then called the *isobaric adiabatic flame temperature*. Its value depends on the products composition, therefore the equivalence ratio as well. Its dependence for different fuels at Standard Temperature and Pressure condition (STP) is shown in Fig. 2.3.

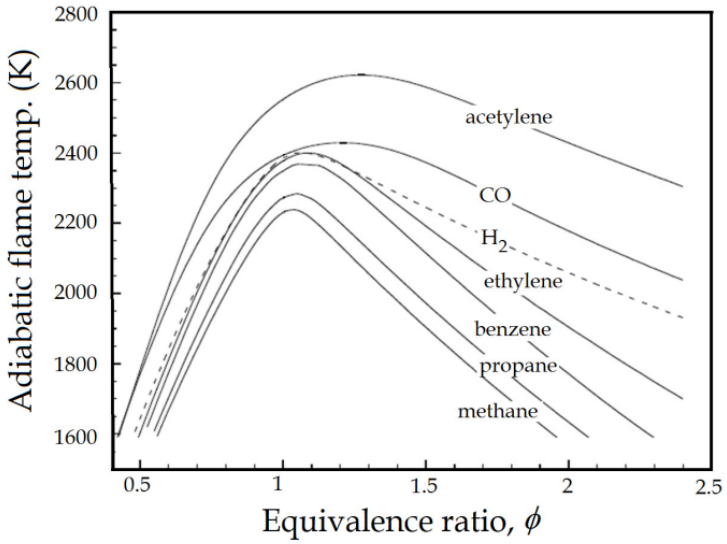

Figure 2.3: Adiabatic flame temperature at STP; source [28]

As one can see, the maximal temperatures are reached around the equivalence ratio equal to one ($\phi = 1$). It means, choosing leaner, premixed mixture keeps the flame

temperature way lower than the maximum.

2.2 Premixed vs Diffusion Flames

Depending if the fuel and air are mixed before entering the combustion chamber or mixed by diffusion after doing so, the flame can be classified as *premixed* or *diffusion flame*. The flame shapes of both types are presented in the Fig. 2.4a.

(a) Luminous images of the premixed and diffusion flames at the same air and fuel flow rates; source [42]

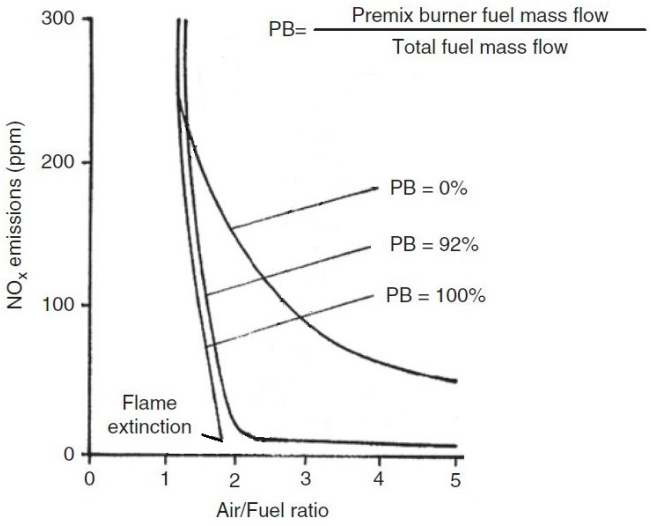

(b) NOx emissions for diffusion ($PB = 0\%$), premixed ($PB = 100\%$) and partially premixed ($PB = 92\%$) flames vs. normalized Air/Fuel ratio $\lambda = \frac{1}{\phi}$; source [19]

Figure 2.4: Premixed vs. diffusive flames

Historically, early engines used pure diffusion combustion with equivalence ratio at the air-fuel interface $\phi \approx 1$. It had to be coupled with further dilution air streams to complete the combustion and lower the flow temperature to reach the values suitable for the turbines (because of high combustion temperatures, see Fig. 2.3) [38]. A main advantage of this setting is the stability of the flame. Simplicity (linked to stability) is also a strong point - diffusion flame systems are easier and cheaper to install (the premixer is not needed).

In diffusion combustion the equivalence ratio (and therefore temperature distribution) is far from even: rich and lean regions of the combustion volume exist simultaneously. As we are dealing with wide variety of thermodynamic conditions, the chemical kinetics and emissions have to be evaluated for each region individually. In case of diffusion flames, we are observing local hot flame spots - the equivalence ratio at the flame front is large. As high temperatures favour thermal NOx formation mechanisms (see section 2.6), we

are witnessing increased NOx emissions - see Fig. 2.4b.
Another problem associated with combustion of a non-premixed flow is the risk of low efficiency - with not careful design considerable amount of fuel might remain unburned. In higher ϕ zones, due to lack of oxidizer, substantial amounts of CO are being produced.

On the other hand, in case of premixed combustion, the equivalence ratio (hence the temperature) distribution is much more uniform. Assuming ideal premixing and no heat loss, the flame temperature would be constant throughout all the domain. Even though ideal conditions are never the case, premixing successfully deals with NOx emission problems. We are not observing such a temperature gradient, the local hot spots' creation is being suppressed. Thus NOx emissions are decreased.
Premixing homogenizes not only the temperature, but also equivalence ratio throughout the domain, so in case of well adjusted and precisely fixed ϕ (temperatures are high enough) ensures efficient combustion.

A potential threat for the premixed combustion system is a flashback phenomenon. Flashbacks occur when the burning velocity becomes larger than the incoming flow velocity. As a consequence, the flame proceeds upstream from its desired zone and reaches the premixing elements.
Another occurrence hazardous for the premixed flame gas turbines is the spontaneous ignition. It is a process, where combustible mixture is being ignited without an external source of ignition (flame or spark). It should be strictly avoided, since it might damage the fuel preparation zone and cause large pollution.
Low stability of the premixed flame causes another threat: the combustion dynamics - high amplitude pressure oscillations in the combustor.
Finally, the flame can also be extinguished - this phenomenon is called *blow off*.

Taking into consideration mentioned factors, modern gas turbines are using main premixed flames, supported by a small pilot flame (up to 10% of fuel mass flow). Some manufacturers use diffusion pilot for stabilisation, while the others have fully premixed combustion. An example of the second group is Advanced Combustion system for high Efficiency (ACE) used in Siemens Energy turbines (Fig. 2.5) [26]. This combustor is modeled later in the following thesis.

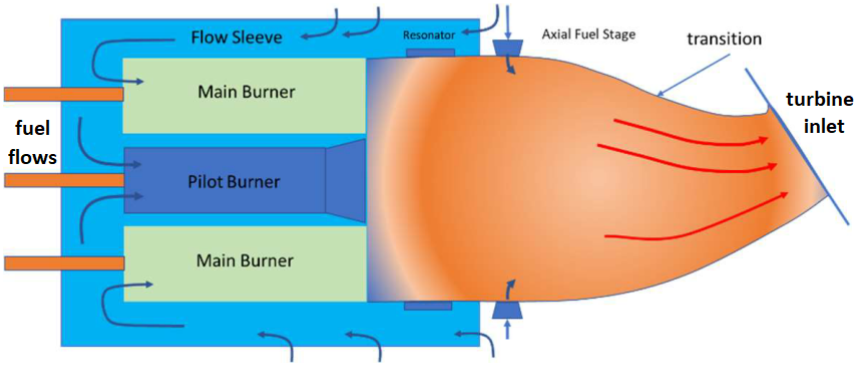

Figure 2.5: Schematic drawing of ACE system; source: [26]

In this model, premixed fuel-air flow is injected to the *Pilot Burner*, *Main Burners* and *Axial Fuel Stage* - downstream in the combustor (Fig. 2.5 is a longitudinal section of a cylinder-like combustor, so *Main Burners* and *Axial Fuel Stages* are axisymmetrically distributed).

2.3 Turbulent Premixed Combustion

Taking into consideration the flow velocities both diffusion and premixed flames can be labeled *laminar* or *turbulent*. Turbulent premixed combustion is a phenomenon combing two complex problems - turbulence and chemistry. In case of laminar flames propagation velocity is only specified by thermal and chemical characteristics of the mixture, whereas in case of turbulent flame, the propagation velocity depends also on the fluid flow.

2.3.1 Flame Structure

Let us consider the turbulent flame stabilized over the tube, from which fuel-air mixture is flowing to the atmosphere. When looking at the instantaneous flame fronts at different times, one sees a superposition of highly wrinkled surfaces (Fig. 2.6). Their convolutions are particularly intense near the flame top. They are usually referred to as *laminar flamelets*. By time-averaging the view, one is getting a thick reaction zone, called frequently the *turbulent flame brush*.

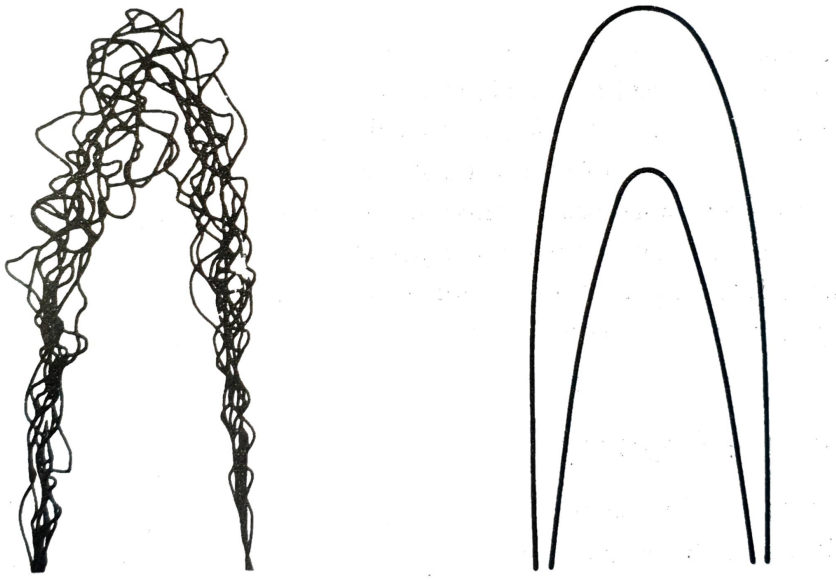

Figure 2.6: Superposition of instantaneous flame fronts acquired at different times (a) and the time averaged flame (b); source: [15]

2.3.2 Flame Regimes

An important concept describing the turbulent premixed combustion is the flame regime. The idea of regimes is based on length scales present in the turbulent flow. They are namely: Kolmogorov scale η - microscale bound up with the smallest eddies dissipating their kinetic energy into the internal one and the integral scale l characterizing the largest eddies. The regimes are specified basing on the relationship of laminar flame thickness l_F with the specific eddy length scale.
Another important parameter necessary to specify the flame regime is the Damköhler number (Da), which is a dimensionless parameter representing the ratio of characteristic flow time to a characteristic chemical time [38]:

$$Da \equiv \frac{\tau_{flow}}{\tau_{chemical}} \tag{2.2}$$

In this study flow time scale is a lifetime of large eddies - $\tau_{flow} \equiv \frac{l}{v'}$; chemical time scale is based on a laminar flame: $\tau_{chemical} \equiv \frac{l_F}{S_L}$ (v' stands for turbulence intensity, S_L is a laminar flame speed).
Second dimensionless number used to describe the flame regimes is Karlowitz number - the ratio of the flame time scales to the Kolmogorov time scale (lifetime of the smallest eddies τ_η) [30]

$$Ka \equiv \frac{\tau_{chemical}}{\tau_\eta} \tag{2.3}$$

The diagram with regimes of turbulent premixed combustion is presented in Fig. 2.7. The parameter on the y-axis is $\frac{v'}{S_L}$ - a ratio of turbulence intensity v' and laminar flame speed S_L. Large values of $\frac{v'}{S_L}$ stand for high turbulence: the flow time scales are smaller than the chemical time scales.
The parameter on the x-axis is $\frac{l}{l_F}$ - ratio of integral length scale and the flame thickness.

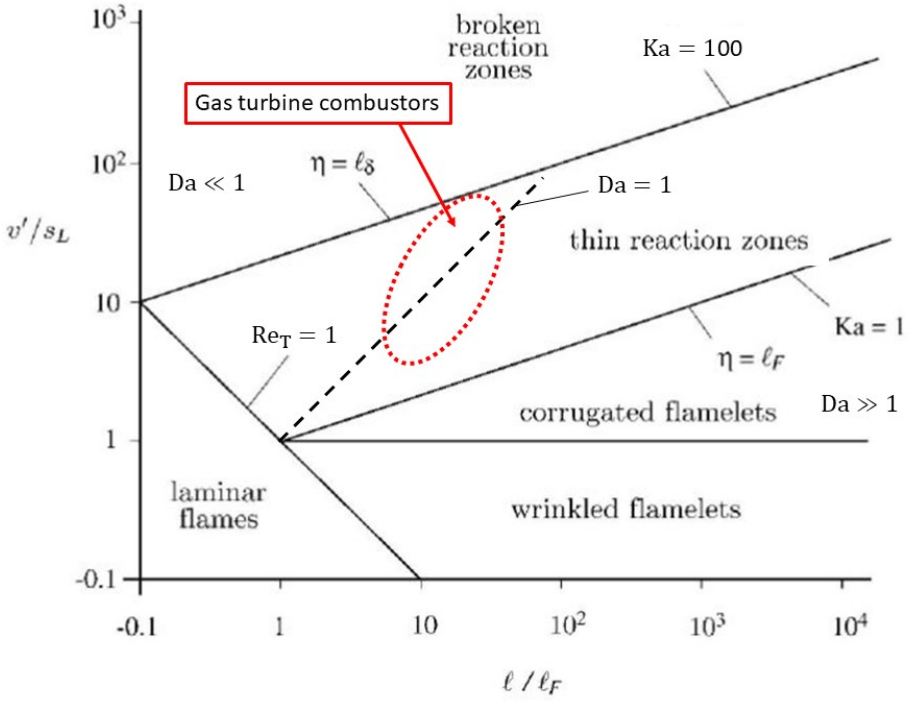

Figure 2.7: Borghi-Peters diagram showing the regimes of premixed turbulent combustion. Premixed combustion in gas turbines lays in the marked area; source [30]

Thin Reaction Zones

The regime of premixed combustion in gas turbines is the *thin reaction zones* (see Fig. 2.7) [21]. This regime is characterised by moderate Da and high turbulence intensities ($v'/S_L \gg 1$). The *thin reaction zones* area on the Borghi-Peters diagram is limited by lines:

- $Re_T = 1$, where Re_T is the turbulent Reynolds number: $Re_T = \frac{v' \cdot l}{S_L \cdot l_F}$ [30] - with this condition it is ensured that the flame is turbulent,
- $1 < Ka < 100$, the flame time scales $\tau_{chemical}$ are larger than τ_η, but not more than 100 times larger.

Figure 2.8 pictures the flame zone consisting of parcels of burned and almost-completely burned gas. The factor limiting the combustion rate is then rate of breaking down unburned gas parcels (to provide sufficient area between hot gases and combustible mixture). In this case it is the turbulence, that controls the process.

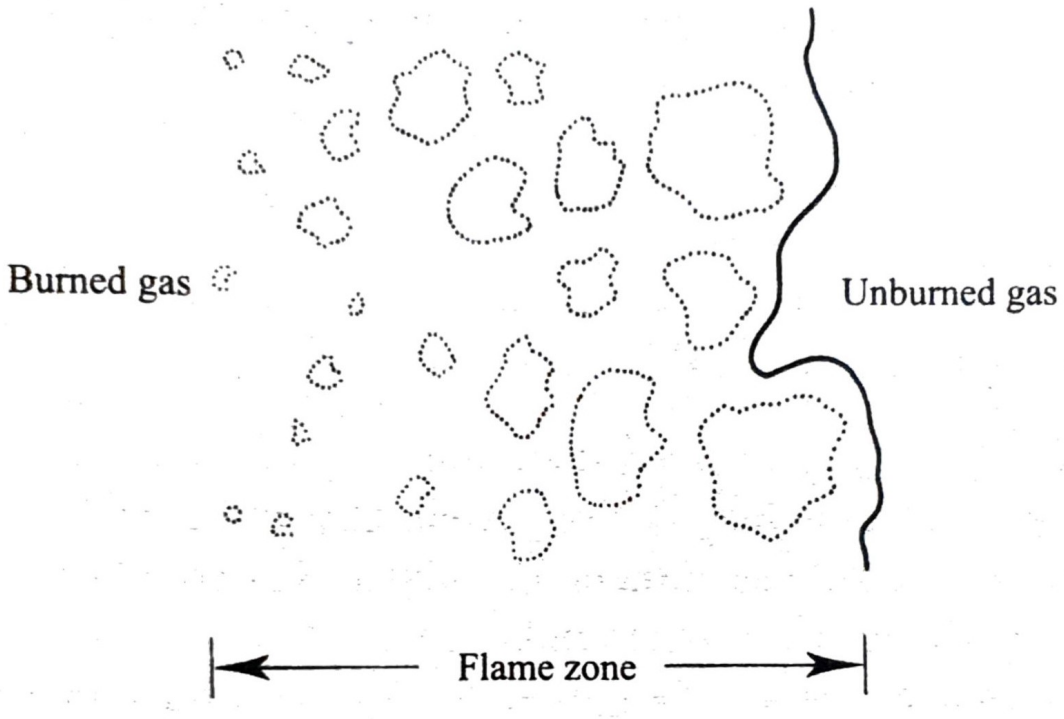

Figure 2.8: Thin reaction zones scheme; source - [38]

2.4 Turbulent Mixing

Turbulent motion intensifies mixing of multiple flows. External fluid introduced in a turbulent region, is being carried and dispersed across the region by all sizes of eddies. In case of larger eddies the entrained fluid is being mostly transported, while smallest ones promote the molecular diffusion.

2.4.1 Gas Turbine Premixer

In modern low-emissions gas turbine combustors the fuel is injected into the air flow, enabling both components to mix before they enter the combustion chamber. The ratio of the fuel to air mass flows is small, usually around $\frac{\dot{m}_{fuel}}{\dot{m}_{air}} = 0.04$ As one can see in the Fig. 2.9 fuel is injected perpendicularly to the main flow downstream of a turbulence generating device. Then, air and fuel flows mix within the tube length (L_{premix}).

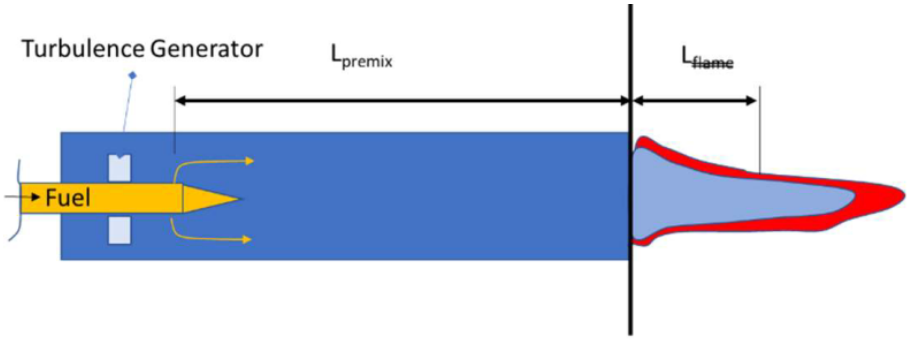

Figure 2.9: Scheme of the gas turbine premixing tube; source [26]

The phenomenon used to model the premixer is a turbulent jet in cross-flow.

2.4.2 Cross Flow Jet

In case of a cross flow jet, various additional vortices are caused by perpendicularity of two flows (see Fig. 2.10a). Due to effective mixing capability this setting is favoured by many gas turbine manufacturers [16].

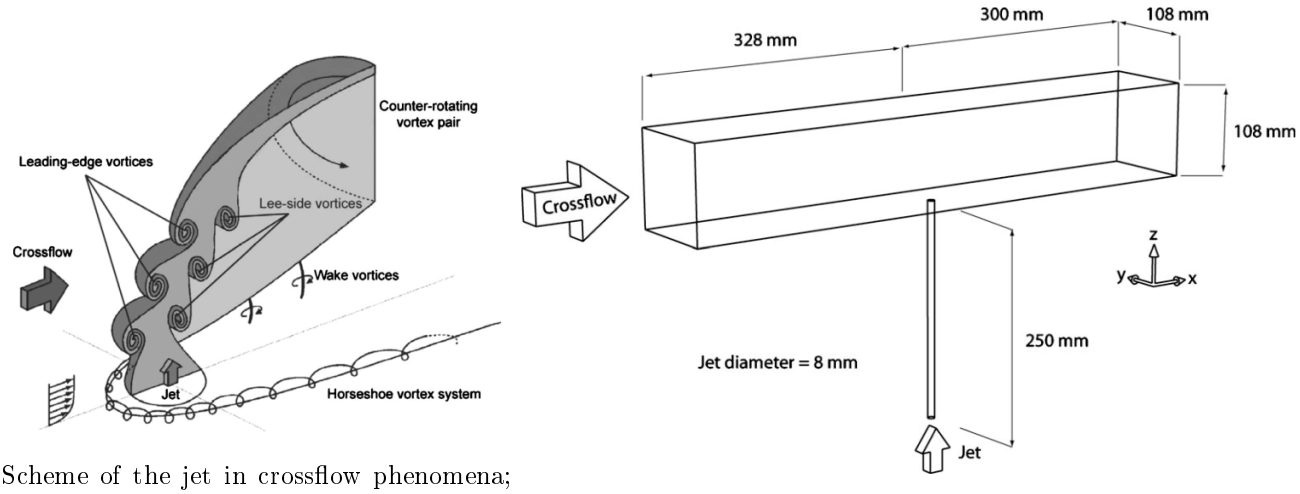

(a) Scheme of the jet in crossflow phenomena; source [16]

(b) Experimental channel setup; source [16]

Figure 2.10: Cross-flow turbulent jets used in mixing modeling

Galeazzo et. al. [16] investigated experimentally the cross-flow jet under highly turbulent conditions (present in the gas turbine engines). Their flow setup is presented in Fig. 2.10b. z axis is a symmetry axis of the injected jet. x axis is parallel to the main flow, with point 0 in the jet injection location. D is a jet diameter. Aerosol particles

(diameter $< 2\mu m$) were injected into both flows, for the use of Particle Image Velocimetry - to get the velocity field. Additionally 5000ppm of NO_2 were added to the jet, for Laser Induced Fluorescence - to see the concentration of the jet-origin fluid in the main flow.

Figure 2.11 presents concentration C and concentration variation $\bar{c'}$ for the cross flow jet at different z/D values: 1.5, 3 and 4.5

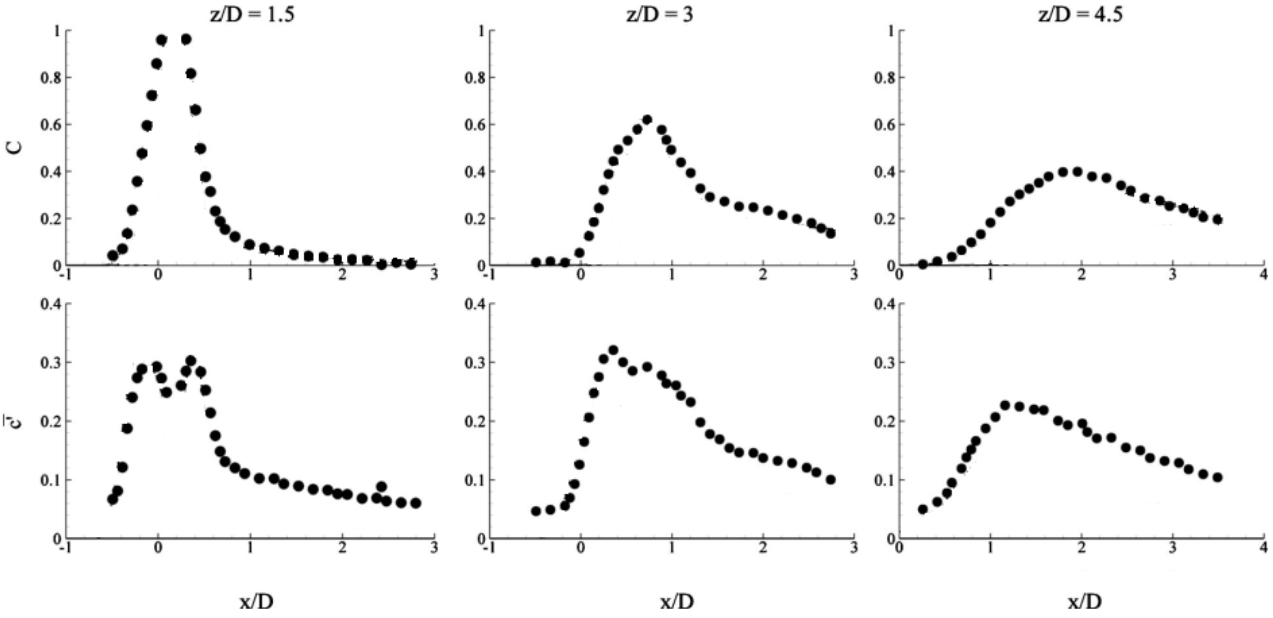

Figure 2.11: Dimensionless concentration C and dimensionless standard variation $\bar{c'}$ - experimental data; source - Galeazzo [16]

Results from Fig. 2.11 show, that when moving in positive directions of x and z axes - the concentration is more uniform (mixed). Same thing happens with concentration variation.

2.5 Chemical Kinetics

The rates of chemical reactions differ in magnitudes and can be comparable to the rates of flow and molecular transport. It plays an important role in controlling the rate of combustion, pollutant formation and elimination. The information about the rate of different reactions is contained in the *chemical kinetics*.

The rate at which fuel F is being depleted can be stated as:

$$\frac{d[X_F]}{dt} = -k_G(T)[X_F]^n \cdot [X_{Ox}]^m \tag{2.4}$$

Where:

- $[X_F]$ and $[X_{Ox}]$ stand for fuel and oxidizer molar concentrations in $[\frac{kmol}{m^3}]$
- $k_G(T)$ is the global rate coefficient (strongly dependent on the temperature)
- variables m and n stand for the reaction order, in case of general reactions - achieved experimentally

Global reaction can be treated as a *black box* for solving several coarse problems, but for understanding what is exactly happening in the system one has to study the elementary reactions that result in many intermediate species. Compilation of all simple reactions and their reaction rates is termed the *reaction mechanism*.

2.5.1 Rate Coefficients' Dependence on Temperature

Rate coefficients of elementary reactions depend on the temperature strongly and non-linearly. According to *Arrhenius Law* [40]:

$$k = A' \cdot exp\left(-\frac{E'_a}{RT}\right) \tag{2.5}$$

Here empirical parameters are: A' - a pre-exponential factor and E'_a - the activation energy - threshold energy level necessary for the reaction's occurrence. The R and T stand for the universal gas constant $R = 8.314\frac{J}{K \cdot mol}$ and temperature respectively. For small activation energy or very high temperatures, the exponent in (2.5) goes to unity. Then the reaction rate depends only on the preexponential factor and is constant.

2.5.2 GRI 3.0 Mechanism

The GRI 3.0 is a natural gas combustion mechanism developed in 1999 by Smith et. al at the Gas Research Institute at the University of Berkeley [20]. It is being widely used in the combustion community. It includes 325 reactions and 53 species with their thermodynamically dependent rate coefficients. Its range of application is [24]:

- Temperature 1000 - $2500K$
- Pressure $10torr$ $(1.33 \cdot 10^3 Pa)$ - $10atm$
- Equivalence ratio 0.1 - 5.0

GRI 3.0 mechanism can be implemented in combustion simulations, as it was done in the following thesis.

2.6 NOx formation mechanisms

A subset of reactions included in Chemical Kinetics are those resulting in NOx production. NOx have several formation mechanisms, highly dependent on the thermodynamic combustion conditions and fuel compositions. The most important pathways for the gas turbine combustors are: thermal, prompt and N_2O oxidation [40]. All three are described below.

2.6.1 Thermal NO

Known also as *Zeldovich NO* (after Yakov Zeldovich, who described the mechanism in 1946 [41]) is consisting of the set of elementary reactions:

$$O + N_2 \xrightarrow{k_1} NO + N \tag{2.6}$$

$$N + O_2 \xrightarrow{k_2} NO + O \tag{2.7}$$

$$N + OH \xrightarrow{k_3} NO + H \tag{2.8}$$

Present in the high temperature regions both in the flame and the post flame flow. The name of the mechanism comes from its strong dependence on the temperature. The reaction's (2.6) rate coefficient ($k_1 = 1.8 \cdot 10^{14} exp(-318kJ \cdot mol^{-1}/(RT)) cm^3/(mol \cdot s)$) requires high activation energy to break the triple bond in the N_2 molecule [40]. Thus its rate is significant only at higher temperatures (above 1700K) - see Fig. 2.12. As steps (2.7) and (2.8) are assumed to be fast ($d[N]/dt \approx 0$), only the first reaction is rate-limiting for the thermal NO formulation [40].

The non-linear rate coefficient dependence on the temperature is presented in Figure 2.12.

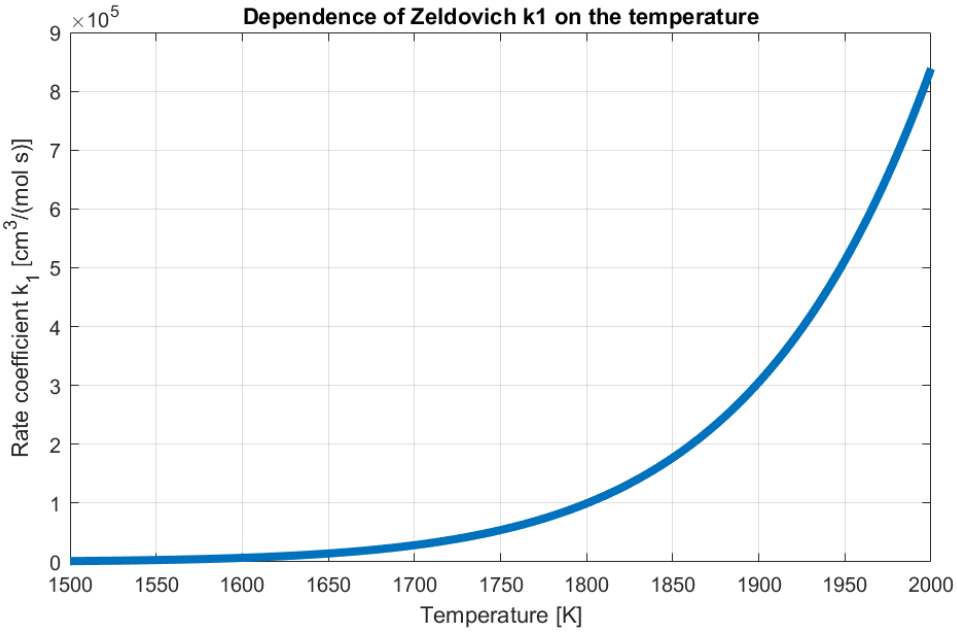

Figure 2.12: Plot of k_1 vs Temperature

2.6.2 Prompt NO

Prompt NO, also known as Fenimore NO (named after scientist who proposed it in 1979 [14]) is another NOx formation pathway. Fenimore stated, that NO is formed from the CH radicals present at the flame front:

$$CH + N_2 \rightarrow HCN + N \tag{2.9}$$

Produced HCN molecule oxidises to NO by undergoing reactions 2.10 - 2.14 [19].

$$HCN + O \rightarrow NCO + H \tag{2.10}$$

$$HCN + OH \rightarrow CN + H_2O \tag{2.11}$$

$$CN + OH \rightarrow NCO + H \tag{2.12}$$

$$NCO + O \rightarrow NO + CO \tag{2.13}$$

$$NCO + OH \rightarrow NO + CO + H \tag{2.14}$$

The nitrogen atom from 2.9 is also taking part in the reaction (2.7). The activation energy of the reaction (2.9) is $75kJ/mol$ ($T_a = 9000K$), whereas the activation energy of (2.6) (thermal NOx) is $318kJ/mol$ ($T_a = 38200K$). Since that Fenimore mechanism is performing even at relatively low temperatures (about $1000K$).

2.6.3 Nitrous Oxide NO

The Nitrous Oxide Pathway [29] is similar to the thermal one, but in this case it is accompanied by a third molecule M (that can be any molecule, often referred to as a *third body*). The outcome is:

$$N_2 + O + M \longrightarrow N_2O + M \tag{2.15}$$

After N_2O is created, it may react with oxygen atom and form NO [29]:

$$N_2O + O \longrightarrow NO + NO \tag{2.16}$$

The activation energy of the reaction (2.16) is only $97kJ/mol$, so low temperature is not an obstacle. In frequently observed conditions the Nitrous Oxide path produces insignificant part of NO [40]. But in case of lean mixture (CH radicals formation suppressed - Fenimore blocked) and low temperature (Zeldovich suppressed) it can play an important role. Quoting Correa [9], it can even become "the major source of NO in lean premixed combustion in gas turbine engines".

2.6.4 Turanyi's corrections to GRI 3.0

The GRI 3.0 mechanism has all the reactions of the mentioned NOx pathways covered. Also the mechanism's range of application is said to lay between $1000K$ and $2500K$. Despite of that, the NOx emissions investigation in higher temperatures ($1800K$) is not performed with satisfying accuracy [1]. In 2017 Turanyi et. al. [8] proposed rate corrections of the NOx producing reactions, resulting in much closer correlation with the experimental results. In the following thesis both mechanisms (with and without Turanyi corrections) are being investigated.

2.6.5 NOx Formation in Gas Turbines

NOx formation in gas turbine combustors was an object of research for decades. In several papers ([6], [12]) the NOx formation is split into two different contributions: *prompt* (fast, formed in the flame) and *postflame* (thermal, happening in hot gases downstream). This distinction is motivated by differences in the turbulence-chemistry interactions. The scheme of the combustor (showing regions of two mentioned contributions) is presented in Fig. 2.13a.

The results in Fig. 2.13b are obtained using 1D perfectly premixed flame models for two values of equivalence ratio: $\phi = 0.571$ and $\phi = 0.653$. The NOx production is represented by the *NOx source term value* - $\dot{\omega}_{NOx}$ - mass of NOx formed per volume and time $[\frac{kg}{m^3 \cdot s}]$ (left axis). Without surprise, one can notice that in case of higher equivalence ratio, NOx source term is higher. It is caused by the simultaneous higher flame temperature (right axis). It is also worth to mention, that in the post flame region the NOx production rate is constant.

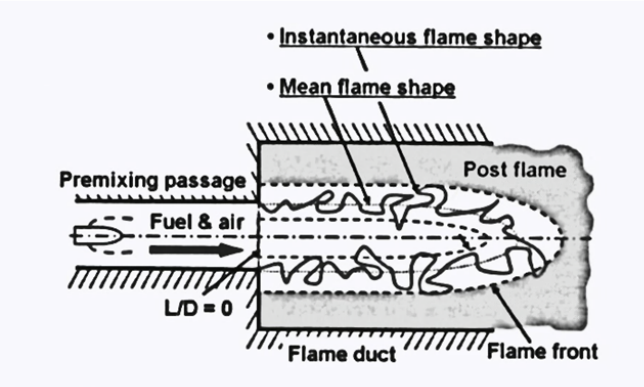

(a) Sketch of a gas turbine combustion system. L/D is a dimensionless coordinate in the main flow direction; source - Dederichs [12]

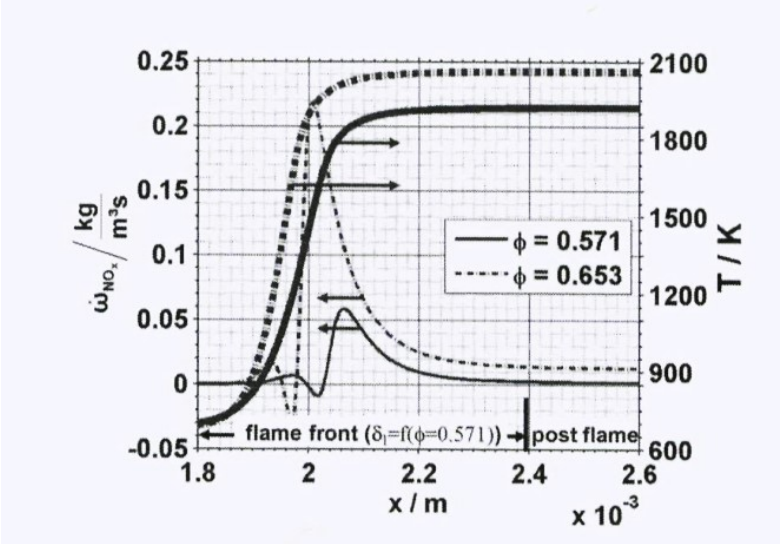

(b) NOx source term and temperature as a function of the laminar flame spread for two exemplary equivalence ratios. Natural gas at 8 bar; source - Dederichs [12]

Figure 2.13: Prompt and postflame NOx

For several decades researchers were investigating the influence of different (other than temperature) thermodynamic parameters on the amount of NOx produced. In case of pressure, a popular assumption is the $\simeq p^{0.5}$ dependency [36]. However, many scientists suggest more complicated dependencies, even with negative powers (decrease in NOx in higher pressures) [5].
In Correa's review paper [10] he suggests that the NOx emissions scale with pressure: $[NOx]_p/[NOx]_{1bar} = p^{\xi}$, where ξ increases from $\xi = 0$ (lean conditions) to $\xi = 0.5$ (at higher ϕ).

2.7 Reactor Network

To describe the changes in the chemical composition of the flow, one can use the concept of reactors. In case of modelling the combustor, a chemical reactor network (CRN) is being used. Among a large variety of reactors, in this study two types of ideal reactors are used in simulating combustion: Perfectly Stirred Reactor (PSR) and Plug Flow Reactor (PFR) [40].

2.7.1 Perfectly Stirred Reactor

Also known as *continous-strirred-tank (CSTR)* is an ideal model, where feed and product flows are continuous and the content of the reactor is perfectly mixed. The temperature and concentration inside the reactor are equal to the outflow conditions. Residence time of each of the flow elements (small fluid parts) may be different. Steady-state operation is assumed, hence there is no time dependence in the mathematical description. PSR scheme is presented in Fig. 2.14.

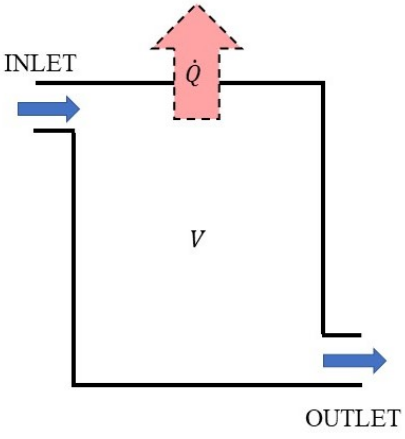

INLET	
Total mass flow:	$\dot{m}$
Mass flow of species k:	$\dot{m} \cdot y_{in,k}$
Energy flow for species k:	$\dot{m} \cdot y_{in,k} \cdot h_{in,k}$

OUTLET	
Total mass flow:	$\dot{m}$
Mass flow of species k:	$\dot{m} \cdot y_{out,k} = \dot{m} \cdot y_{in,k} + \dot{\omega}_k \cdot V \cdot W_k$
Energy flow for species k:	$\dot{m} \cdot y_{out,k} \cdot h_{out,k}$

Figure 2.14: PSR scheme with conservation equations

Governing equations of the PSR (for each species k), forming a set of $K+1$ ordinary differential equations are presented below [17].

Mass balance:

$$\dot{m}(y_{out,k} - y_{in,k}) - \dot{\omega}_k \cdot V \cdot MW_k = 0 \tag{2.17}$$

Heat balance:

$$\dot{m}\sum_{k=1}^{K}(y_{out,k}\cdot h_{out,k} - y_{in,k}\cdot h_{in,k}) + \dot{Q} = 0 \tag{2.18}$$

Variables in equations (2.17) and (2.18) represent:

- $\dot{Q}$ - the reactor heat loss,
- $\dot{\omega}_k$ - molar rate of chemical reaction (production of the k-th species) per unit volume,
- $\dot{m}$ - mass flow in the reactor
- V - reactor volume
- MW_k - molecular weight of the species k
- $y_{in,k}$ or $y_{out,k}$ - mass fraction of species k in the incoming/outgoing flow
- $h_{in,k}$ or $h_{out,k}$ - specific enthalpy of species k in the incoming/outgoing flow

The nominal residence time (τ_{res}) can be calculated using the product mixture density (ρ, computed in (2.20) from the ideal gas law), reactor volume (V) and the mass flow rate ($\dot{m}$):

$$\tau_{res} = \frac{\rho V}{\dot{m}} \tag{2.19}$$

$$\rho = \frac{P\hat{MW}}{RT} \tag{2.20}$$

Where $\hat{MW}$ is a mean molecular weight, R is a universal gas constant, P - the pressure, T - the temperature. In this thesis project PSRs will be used as a mixture ignition reactor - they will represent the flames.

2.7.2 Plug Flow Reactor

Another type of reactor is the plug flow reactor (also known as *piston flow reactor*). It is usually visualized as a long pipe, with steady and uniform axial flow (see Fig. 2.15). There is no mixing in the direction of the flow. Residence time for each fluid element is equal. Additional assumptions are the friction-less flow and ideal-gas behaviour [40].

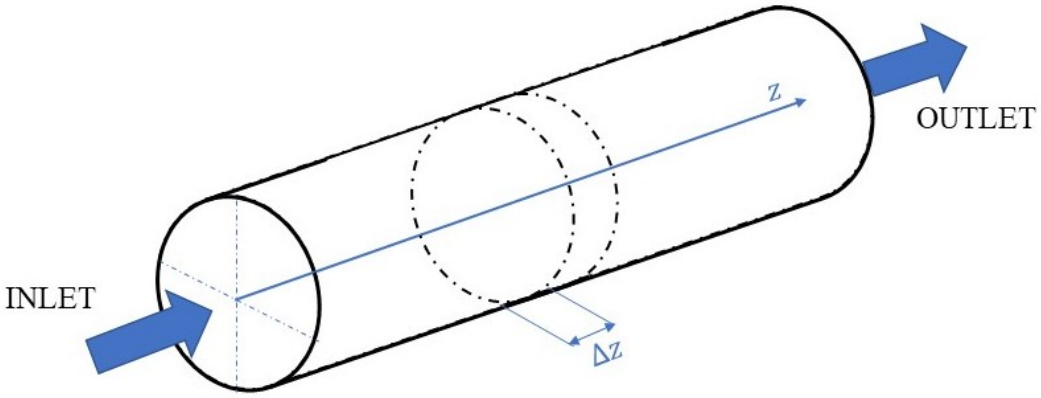

Figure 2.15: PFR scheme with infinitesimal control volume Δz

The cross-sectional area is not necessarily constant ($A(z)$) - model might represent simple pipe as well as a nozzle or diffuser. The axial position of all particles in a certain, moving cross-section (z) is computed using (2.21).

$$z = t \cdot v_z \tag{2.21}$$

Here, the t denotes time elapsed since the clump of fluid entered the reactor (age of the material point at z) and v_z stands for velocity of the fluid. The complete mixing is being assumed in each cross-section, so the concentration of species k is a function of only z: $y_k(r, \phi, z) = y_k(z)$.

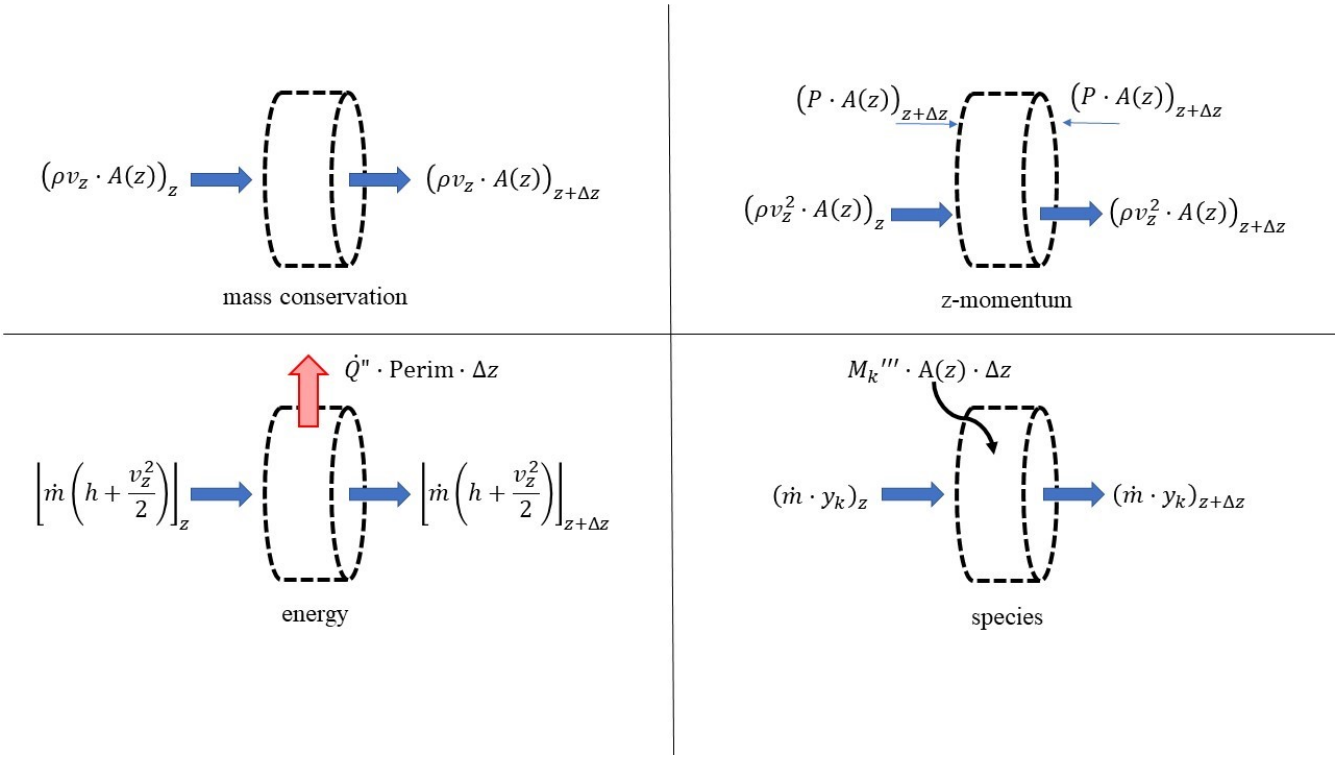

Figure 2.16: Infinitesimal control volume Δz with fluxes of mass, z-momentum, energy and species

Taking into account infinitesimally small control volume balances shown in Fig. 2.16, governing equations are stated [38]:
Mass conservation:

$$\frac{d\left(\rho v_z A\right)}{dz} = 0 \tag{2.22}$$

Momentum conservation in z direction

$$\frac{dP}{dz} + \rho \cdot v_z \frac{dv_x}{dz} = 0 \tag{2.23}$$

Energy conservation

$$\frac{d\left(h + v^2{}_z/2\right)}{dz} + \frac{\dot{Q}''\mathcal{P}}{\dot{m}} = 0 \tag{2.24}$$

Species conservation

$$\frac{dy_k}{dz} - \frac{\dot{\omega_k} MW_k}{\rho v_z} \tag{2.25}$$

Where additionally:

- A - area of the pipe cross section $[m^2]$

- $\dot{Q}$" - heat flow through the wall $[\frac{W}{m^2}]$
- $\mathcal{P}$ or $Perim$ - local perimeter $[m]$

In this work, plug flow reactors are placed after the PSR and used to model the post flame region in the combustion chamber.

2.8 Turbulent Mixing Modelling

The turbulent mixing takes place both in the premixer and downstream of the flame. Modelling the mixing in the whole combustor is necessary to accurately simulate the turbulent premixed combustion.

2.8.1 Unmixedness Definition

Unmixedness is the variable describing quantitatively the mixing quality of the flow. Let us consider a volume consisting of a large number of smaller, same sized (elementary) volumes. Each elementary volume has its own concentration of species k. The set of concentrations for each small element can be then presented on histograms, which are treated as concentration pdf. An example of CFD-based (CFD - Computational Fluid Dynamics), non-perfectly premixed fuel mass fraction pdf is presented in Fig. 2.17. The variable on the x-axis is fuel mass fraction (Y_{fuel}). If the mixing was perfect, the histogram would be a single bar with all volumes having the same concentration.

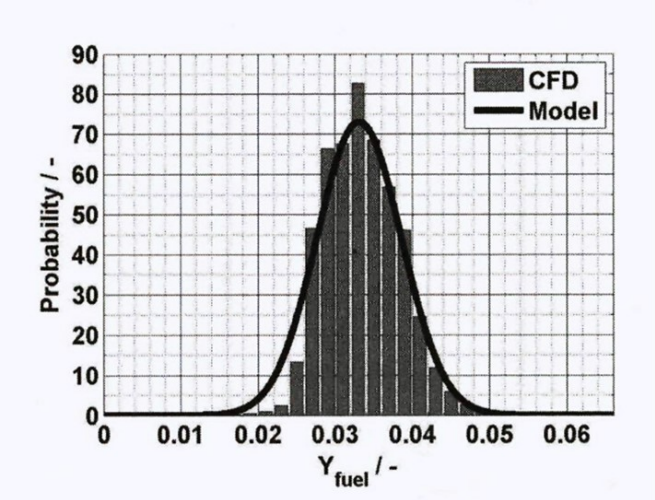

Figure 2.17: CFD-based probability (sampled over generic flame front) and its Gaussian distribution approximation; source [12]

Among many possible definitions of unmixedness (U), in our considerations we will use the simple one - employing the standard deviation (σ) and mean value of mass concentration of particular species in the flow ($\bar{y}$).

$$U = \frac{\sigma}{\bar{y}} \tag{2.26}$$

It is worth mentioning that unmixedness can be spatial (steady state) or spatio-temporal (accounting for concentration changes in time). In this thesis only the steady state unmixedness is treated.

2.8.2 Monte Carlo Algorithm

Monte Carlo is a computational algorithm, that uses random samples to obtain results. It can be employed to solve stochastic problems, by simulating their random processes. In this study, mixing is done using the Monte Carlo algorithm.

In this approach, the flow in the combustor is divided into thousands of smaller parts - particles of the same mass. Each particle has its own values of composition and enthalpy. Let us consider the case of mixing two separate flows of pure CH_4 and pure oxidizer. Both of them are divided into a number of particles of mass $m_{particle}$: N_{fuel} and N_{air}. Initially, all fuel particles have their properties (enthalpy and mass composition vectors) equal to: $h = h_{CH_4}$ and $y_{CH_4} = 1$. For pure air stream, the properties are: $h = h_{air}$ and $y_{CH_4} = 0$. Mixing phenomenon is being modelled by observing the interactions between pairs of particles.

2.8.3 Modified Curl's Model by Pope

A model used to simulate mixing in the combustor is Modified Curl's model. The idea was firstly proposed by Curl in 1963 [11] for the diffusion mixing and modified by Janicka in 1979 [25]. Later several improvements were delivered by Pope [31]. Those enabled using it in case of turbulent mixing.

To simplify the explanation, let us treat only one property - the concentration. For simple case: $t = 0$, the set of particles is consisting of two same sized packets of fluid with concentrations equal to y_1 and y_2. The mean concentration is $\frac{1}{2}(y_1 + y_2)$. A normalized concentration ψ parameter is being introduced:

$$\psi = 2 \cdot \frac{y - \frac{1}{2}(y_1 + y_2)}{y_1 - y_2} \tag{2.27}$$

The normalized concentrations for two mentioned packets of fluid are: $\psi_1 = 1$ and $\psi_2 = -1$. The mean concentration is then $< \psi >= 0$, initial variance $< \psi'^2 >= 1$.
Initial pdf of ψ, is

$$p(\psi, t = 0) = \frac{1}{2}\delta(1 - \psi) + \frac{1}{2}\delta(1 + \psi) \tag{2.28}$$

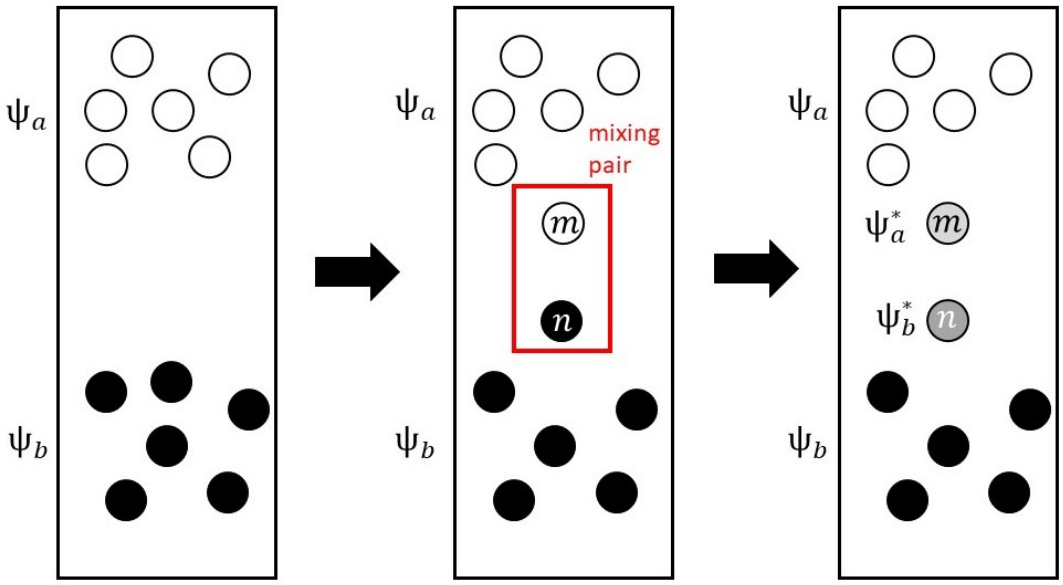

Figure 2.18: Modified Curl Model mixing scheme

Here first delta function stands for fluid packet with $\psi = 1$ ($y = y_1$), while the second corresponds to $\psi = -1$ ($y = y_2$). For time $t > 0$ standard deviation σ ((2.29)) starts to decrease. ψ can obtain values only in the range $-1 \leq \psi \leq 1$.

$$\sigma^2 = \int_{-\infty}^{+\infty} \psi^2 \cdot p(\psi) d\psi \tag{2.29}$$

A stochastic description of the model is following. The total number of particles is N. The $\omega_{decay} = \frac{1}{\tau_{mix}}$ is assumed to be a constant rate of the standard deviation decrease. The model is evolving through small time steps δt (much smaller than the residence time $\delta t \cdot \omega_{decay} \ll 1$). Two particles are randomly selected from the set. Number of selected pairs N_p is computed using $N_p = 3 \cdot \delta t \cdot \omega_{decay} \cdot N$ (constant 3 is suggested by Pope). Let us consider two particles in a pair (denoted by superscripts m and n) - see Fig.2.18. Their ψ values before mixing are (2.30) and (2.31).

$$\psi^{(m)}(t) = \psi_a \tag{2.30}$$

$$\psi^{(n)}(t) = \psi_b \tag{2.31}$$

After one time step, the ψ values are: ψ_a^* for particle m and ψ_b^* for particle n:

$$\psi_a^* = \psi^{(m)}(t + \delta t) = (1 - \Lambda)\psi_a + \frac{1}{2}\Lambda(\psi_a + \psi_b) \tag{2.32}$$

$$\psi_b^* = \psi^{(n)}(t+\delta t) = (1-\Lambda)\psi_b + \frac{1}{2}\Lambda(\psi_a + \psi_b) \tag{2.33}$$

The parameter $\Lambda \in (0,1)$ is a random variable of continuous pdf. The mixed pair of particles is returned to the set.

This procedure is repeated N_p number of times.

2.9 Unmixedness Impact on NOx formation

The quality of mixing in the combustor has large impact on the nitrous oxides emissions. When discussing the unmixedness impact on NOx formation, most of researchers are in agreement: poorer mixing results in higher emissions. The explanation of this behaviour is intuitive: in situation of deficient mixing there are several pockets of leaner and richer mixture. As mentioned in 2.1.1, the flame temperature is strongly dependent on the equivalence ratio. Since NOx emissions are greatly influenced by the temperature (especially with Zeldovich path - see Fig. 2.12), the production in leaner and richer pockets will differ.
Even though the NOx formation is smaller in lean volumes, due to strongly nonlinear dependence on the temperature overall NOx emissions are higher.

In 2013 Dederichs et. al. [12] investigated the NOx emissions for a given global burning temperature and premixing quality. They constructed a 1D combustion model, that delivered NOx production prognosis basing on fuel mass fraction pdfs. Later, they compared the results with experimental data. Due to difficulties with measuring the unmixedness in the actual setup, the U value was estimated in adequate transient and steady state CFD simulations. Two versions of unmixedness were examined : steady state-based *spatial* U, and *spatiotemporal* U computed using transient simulation.
The scheme of investigated can-type combustor is presented in Fig. 2.13a.

Dederich's results are plotted in Fig. 2.19 One can see, that the impact of unmixedness is non-linear. The sharp increase of emissions occurs for $U > 0.2$. Hence this value indicates the level of premixing sufficient for low NOx emissions. Another message from Dederich's results is that for more accurate estimations the spatio-temporal unmixedness has to be taken into account.

Schlegel et. al. [33] also investigated NOx formation with different unmixedness levels. Their results are presented in Fig. 2.20 (the conditions were: inlet temperature $300°C$, $\phi = 0.5$.).

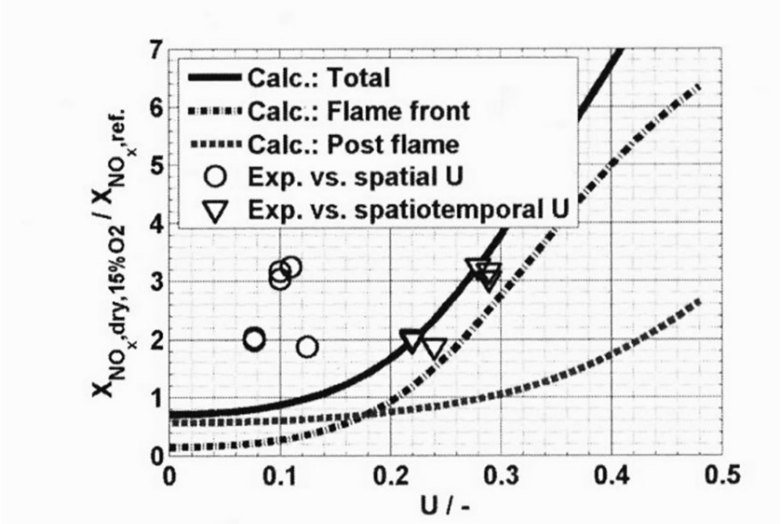

Figure 2.19: Measured NOx emissions related to different CFD-based unmixedness parameters and comparison against the modeled emissions; source - Dederichs [12]

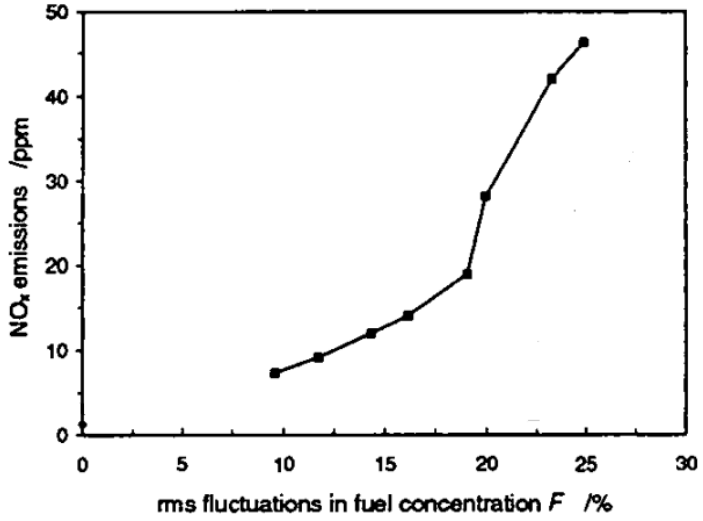

Figure 2.20: Measured NOx emissions at the combustion chamber exit vs. "rms fluctuations in fuel concentration" - basically unmixedness; source - Schlegel [33]

A non-linear NOx emissions behavior is observed - there is a sharp increase around $U = 0.2$ similar to the one in Fig. 2.19.

According to [6] NOx emissions in the postflame region are approximately three times more sensitive to unmixedness than prompt ones. The reason for this behaviour is that the NOx pathway dominant downstream of the flame is the thermal one 2.6.1.

Even though unmixedness is considered undesirable from the NOx emissions' point of view, one should keep in mind that some degree of U is necessary for flame stabilization [6]. [12] points out also risk of flashback, autoignition, pressure drop and limited space as other reasons for desired $U \neq 0$.

2.10 Probability Density Function Approximations

The concentration probability density function after not ideal mixing can be approximated by different bell-shaped distributions. One of them is the beta distribution.

2.10.1 Beta Distribution

It is a distribution fully specified by variate β of two parameters: v and ω [13]. Depending on those two it can be a bell-like (for $v > 1$ and $\omega > 1$ - Fig. 2.21a), U-shaped (for $v < 1$ and $\omega < 1$ - Fig. 2.21b) or J-shaped (for $(v-1)(\omega-1) < 0$ - Fig. 2.21b) curve.

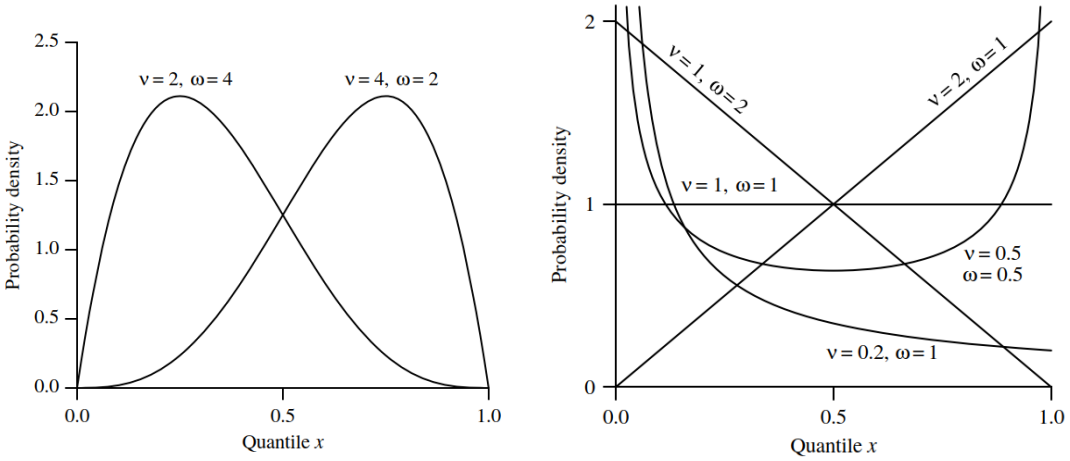

(a) Bell-shaped beta pdf

(b) U- and J-shaped beta pdf

Figure 2.21: Possible shapes of the beta distribution, source: [13]

One of the advantages of beta distribution is the range matching the range of mass fraction - $0 < x < 1$. It prevents from working with non-physical mass fractions: negative and larger than one. Another is the possible skewness of the pdf - the beta distribution produced in turbulent mixing is not necessarily symmetric (what is being seen in the experimental results [27]). Additionally U-shaped pdf can approximate double Dirac function (the initial pdf of two flows, before mixing).

Main characteristics of the beta distribution are gathered in Table 2.1.

Table 2.1: Main characteristics of the beta distribution

Parameter	Value
Range	$0 \leq x \leq 1$
Shape parameters	β: $v > 0$, $\omega > 0$
Probability density function	$\frac{x^{v-1}(1-x)^{\omega-1}}{\int_0^1 u^{v-1}(1-u)^{\omega-1}\,du}$
Mean $\bar{x}$	$\frac{v}{v+\omega}$
Variance σ^2	$\frac{v\omega}{(v+\omega)^2(v+\omega+1)}$
$v = f(\bar{x}, \sigma)$	$v = \left(\frac{1-\bar{x}}{\sigma^2} - \frac{1}{\bar{x}}\right) \cdot \bar{x}^2$
$\omega = f(\bar{x}, \sigma)$	$\omega = v\left(\frac{1}{\bar{x}} - 1\right)$

Chapter 3

Combustor Model

3.1 GeneAC structure

GeneAC is a proprietary 1D tool used to model combustion systems. It is employed by Siemens Energy researchers to obtain additional information about the system response for changing the flow parameters. GeneAC is an early-design-stage computationally efficient alternative for costly CFD analyses. Examples of response analysed by the tool are NOx and CO emissions.

GeneAC is used to compute both the flow pressure distribution and chemical kinetics (with the specified mechanism). So each reaction can be simulated in the approximated thermodynamic conditions present in the combustor.
Despite the availability of pressure computations, due to the small impact of the pressure drop (around 5%) on the chemical reactions, it was decided to be neglected. The total pressure was assumed to be constant throughout all the elements. With known mass flows of the mixture, the system was fully described.

GeneAC combustor models examined in this thesis are consisting from blocks of reactors and their connectors presented below:

- Inlet element - upstream element containing boundary conditions of the system. The inputs are: fuel and air mass flows, composition, temperature, total pressure and the air humidity.
- PSR - Perfectly Stirred Reactor (see 2.7.1), used to model ignition. Input is the volume (therefore the residence time).
- PFR - Plug Flow Reactor (see 2.7.2), used to model post-flame combustion. User definable inputs are geometrical: length (therefore residence time) and inlet and outlet cross-sectional areas (if equal - reactor is modelled as a cylinder, if not - cone section.
- Merger - element used to combine two flows. Used to structure the model. It is a simple connector, with no mixing taking place.

- Outlet - downstream boundary condition. It has no variables to be set.
- Pipe - element used to model the premixer before adding the *prescribed pdf* function. The inputs were the same as in the PFR (the difference with the PFR is lack of reactions in the pipe).

3.2 Monte Carlo in GeneAC

After a successful run of the bulk flow analysis, an additional Monte Carlo simulation is carried out. It is used to account for non uniformity of the mixture.

Instead of simulating chemical kinetics of the bulk mass flow, the mixture is divided into same-mass small flow elements (particles). Particles may differ in composition and enthalpy. Aside from reactions, those particles can exchange properties with each other (to represent mixing in an actual combustor). A group of particles of the flow is called a *particle cloud*.

In the Monte Carlo analysis, the particles are not characterised with velocity. Their movement is described by residence times in each reactor. Those have already been computed in the bulk analysis.

Each particle has four properties:

- mass m_p in $[kg]$, uniform for all the particles,
- enthalpy H_p in $[J]$, constant throughout the reaction, changeable only by mixing,
- mixture fraction f_p $[-]$, constant in the reaction, changeable only by mixing,
- a vector of mass fractions $\overrightarrow{y_p}$ [-], changing when particle undergoes a reaction and in mixing.

3.2.1 Mixture Fraction

Mixture fraction as a particle property was added as a response to the need of tracking the unmixedness downstream of the flame. Previously, the unmixedness of the mixture was computed as:

$$U_{CH4} = \frac{\sigma_{CH4}}{\bar{y}_{CH4}} \tag{3.1}$$

Where σ_{CH4} is a standard deviation of the $CH4$ mass fraction and $\bar{y}_{CH4}$ is a mean particle $CH4$ mass fraction. This definition of U allowed an insight to the pdf only upstream of the flame. Therefore a new, reaction independent variable was introduced - the mixture fraction. The mixture fraction (f) is a ratio of mass flow of the fuel to the mass flow of the dry mixture:

$$f = \frac{\dot{m}_{fuel}}{\dot{m}_{fuel} + \dot{m}_{air,dry}} \tag{3.2}$$

For pure methane cases presented in the thesis: $\dot{m}_{fuel} = \dot{m}_{CH4}$.

The mixture fraction is assigned to each particle in the *Inlet* element. It can change only by means of mixing with other particles (the mean mixture fraction of the particle cloud is constant through the whole system).

Then, the created particle cloud passes through the reactors, to eventually go to the outlet element (where their NOx concentration is examined).

3.2.2 Mixing

As the Monte Carlo analysis simulates mixing, it requires an additional input for the *pipe* element, *PSR* and *PFR* - mixing time scale τ_{mix}. Depending on the quality of mixing in a certain reactor its mixing time scale can be small (good mixing) or large (worse mixing conditions). The method of choosing appropriate values is described in section 3.5.

The *pipe* element is used only for mixing (simulating the premixer). When a particle cloud enters the *PSR*, *PFR* or the *pipe* element, it is being mixed by employing the Modified Curl Model (see 2.8.3) [31].
Firstly, the number of mixing pairs is being computed:

$$N_{mix} = 3 \cdot \frac{\tau_{mix}}{\tau_{res}} \cdot N \tag{3.3}$$

where τ_{mix} is the mixing time scale in the reactor/pipe (determined by the turbulent interactions), τ_{res} is the reactor/pipe residence time and N is a number of particles in the cloud. The source of the constant 3 is described in the 2.8.3.
Then, each randomly picked pair of particles exchanges its enthalpy, mixture fraction and mass composition vector according to:

$$\psi^{1,new} = (1-\Lambda) \cdot \psi_p^{1,old} + \frac{1}{2}\Lambda \left(\psi_p^{1,old} + \psi_p^{2,old}\right) \tag{3.4}$$

$$\psi_p^{2,new} = (1-\Lambda) \cdot \psi_p^{2,old} + \frac{1}{2}\Lambda \left(\psi_p^{1,old} + \psi_p^{2,old}\right) \tag{3.5}$$

where: $\psi_p^{i,new}$ - a mixing scalar property (enthalpy or mixture fraction) of *particle i* after mixing, $\psi_p^{i,old}$ - a mixing scalar property of *particle i* before mixing, Λ - a random number from range $(0, 1)$.

The mass fraction vectors are also updated using factor Λ:

$$\overrightarrow{y_p^{1,new}} = (1-\Lambda) \cdot \overrightarrow{y_p^{1,old}} + \frac{1}{2}\Lambda \left(\overrightarrow{y_p^{1,old}} + \overrightarrow{y_p^{2,old}}\right) \tag{3.6}$$

$$\overrightarrow{y_p^{2,new}} = (1-\Lambda) \cdot \overrightarrow{y_p^{2,old}} + \frac{1}{2}\Lambda \left(\overrightarrow{y_p^{1,old}} + \overrightarrow{y_p^{2,old}}\right) \tag{3.7}$$

where $\overrightarrow{y_p^{i,new}}$ is a *particle i* mass fraction after the mixing and $\overrightarrow{y_p^{i,old}}$ - before the mixing. After being mixed, the particle pair is put back into the particle cloud and both particles can mix again with other particles.
In the reactors particles firstly mix and then they react (with respect to the reactor formulae).

As an effect of mixing, the mixture fraction pdf changes when passing through the reactor/pipe element. An example of this evolution is presented below (Figure 3.1). In this case particle cloud of initial beta-pdf $U \approx 20\%$ (see 3.2.3) is subjected to mixing with $\tau_{mix} = 3ms$. The evolution of the pdf is captured at residence times $0ms$, $2ms$, $4ms$ and $6ms$. The distribution is getting narrower with increase of the residence time.

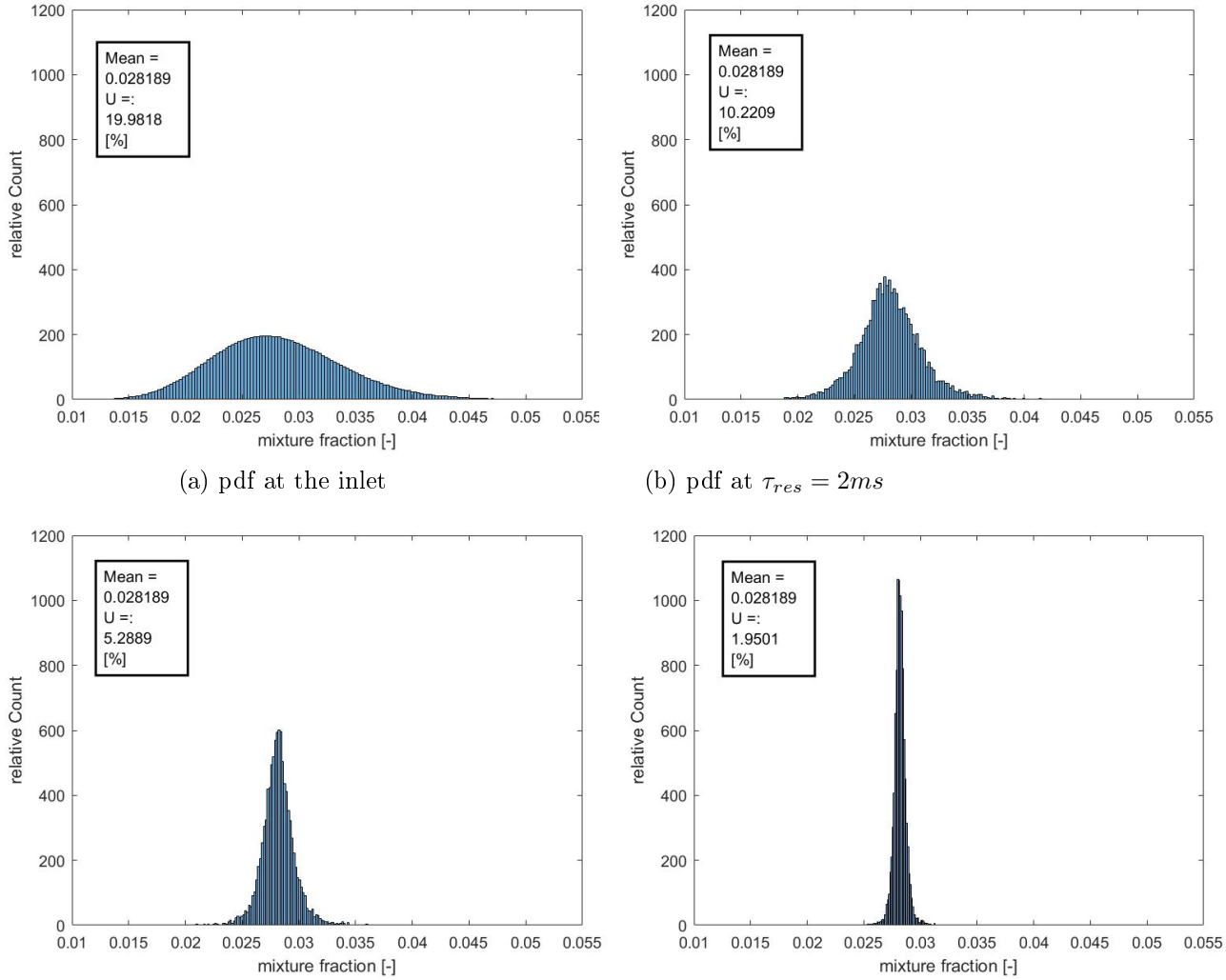

(a) pdf at the inlet

(b) pdf at $\tau_{res} = 2ms$

(c) pdf at $\tau_{res} = 4ms$

(d) pdf at $\tau_{res} = 6ms$

Figure 3.1: Mixture fraction pdf evolution while mixing ($\tau_{mix} = 3ms$)

3.2.3 Prescribed pdf function

Before adding a prescribed pdf function, user had to simulate the premixing of fuel and oxidizer flows. In this scenario a premixer sub-model was consisting of two inlet elements, a merger (to combine two flows) and a pipe element. Scheme of a premixer sub-model is presented in Fig. 3.2 - in the lower part of the image.
The mixing of fuel and oxidizer took place in the pipe. It was simulated with use of Curl turbulent mixing model with mixing time scales *brute-force* adjusted to match the desired unmixedness in the premixer outlet (taken from the CFD).

Applying the mixing model in the pipe was unreliable: the unmixedness of the particles leaving the premixer was showing fluctuations of several percent points between the simulations. To prevent this issue to affect the results, the pdf at the flame was presumed. The prescribed pdf function was added. Thanks to this feature, user is able to start a simulation (in the inlet element) with the mixture fraction unmixedness and pdf shape exactly as expected in the flame front.

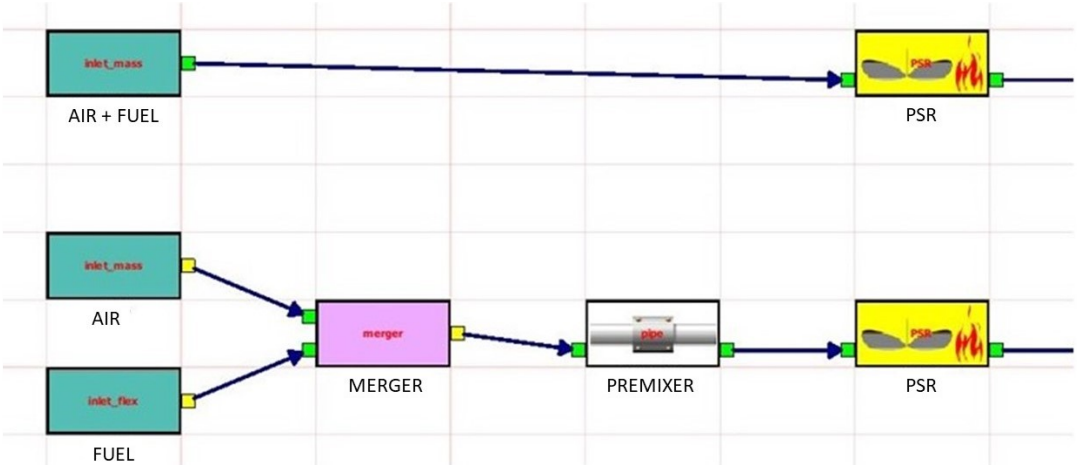

Figure 3.2: Inlet element with prescribed mixture fraction pdf (top) and simulating the premixer (bottom).

The only additional input required in the inlet element is the flame front unmixedness U_D (see 3.5.4).

The mean mixture fraction ($\bar{f}$) of the mixture is computed from the total fuel and oxidizer mass flows:

$$\bar{f} = \frac{\dot{m}_{fuel}}{\dot{m}_{fuel} + \dot{m}_{air}} \tag{3.8}$$

As the inlet pdf is assumed to be a beta-distribution (see 2.10.1), its shape parameters v and ω are computed using following equations:

$$std(f) = U_D \cdot \bar{f} \tag{3.9}$$

$$var = (std(f))^2 \tag{3.10}$$

$$v = \left(\frac{1-\bar{f}}{var} - \frac{1}{\bar{f}}\right) \cdot \bar{f}^2 \tag{3.11}$$

$$\omega = v \cdot \left(\frac{1}{\bar{f}} - 1\right) \tag{3.12}$$

Using a beta inverse cumulative distribution function ($f = I^{-1}(x, v, \omega)$ for more explanation see 2.10.1) the $(N \times 1)$ vector of mixture fractions for each particle is created. The incomplete beta function is defined as:

$$I(x, v, \omega) = \frac{1}{B(v, \omega)} \int_0^x t^{(v-1)} \cdot (1-t)^{(\omega-1)} dt \tag{3.13}$$

Where $B(v, \omega) = \int_0^1 u^{v-1} \cdot (1-u)^{\omega-1}$.

Then two *master particles* are being created:

- air master particle - having the particle mass m_p, oxidizer composition $\overrightarrow{y_{ox}}$ and particle enthalpy computed as $H_{p,ox} = h_{ox} \cdot m_p$ $[J]$ (where h_{ox} in $\left[\frac{J}{kg}\right]$ is the specific enthalpy of oxidizer at inlet temperature and pressure). Its mixture fraction is $f_p = f_{ox} = 0$.
- fuel master particle - having the particle mass m_p, fuel composition $\overrightarrow{y_f}$ and particle enthalpy computed as $H_{p,f} = h_f \cdot m_p$ (where h_f is the specific enthalpy of fuel at inlet temperature and pressure). Its wet mixture fraction is $f_p = f_f = 1$.

Using the *master particles* and the particle mixture fractions the inlet particles are created. Their enthalpy and mixture fraction are:

$$H_p = f_p \cdot H_{p,f} + (1 - f_p) \cdot H_{p,ox} \tag{3.14}$$

$$\overrightarrow{y_p} = f_p \cdot \overrightarrow{y_f} + (1 - f_p) \cdot \overrightarrow{y_{ox}} \tag{3.15}$$

Shape of the pdf

To check the quality of approximating the premixer outlet pdf with a beta distribution, a shape comparison with available CFD data was carried out. In Fig. 3.3 there are two histograms showing the mixture fraction distribution in the premixer outlet - prescribed pdf (blue) and CFD (red). The desired unmixedness in this case was $U_D = 9.5\%$.

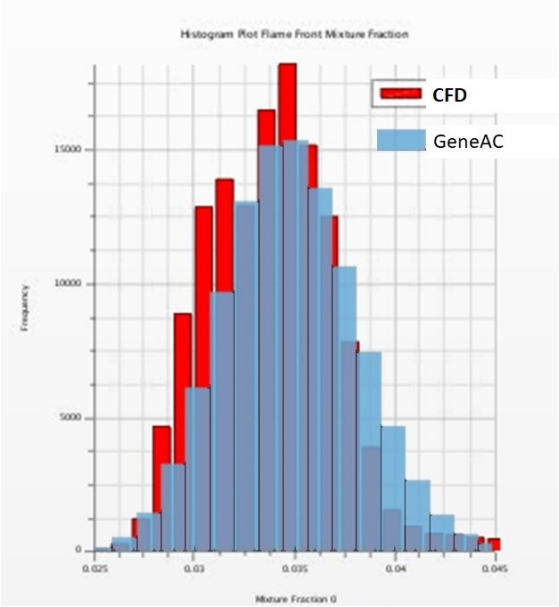

Figure 3.3: Histogram shape comparison of GeneAC prescribed pdf and CFD histogram at the end of the premixer.

The CFD histogram bars were slightly higher in the lean area, but in general beta pdf was decided to be a sufficient approximation.

3.2.4 Reactions

The chemical kinetics of the reactions are computed for each particle separately.
Since simulation of the ignition in the PSR needs a lot of computational time, it is saved by employing the tabulated chemistry. The table of product particles is called the ignition cloud.

The product particles are computed for specific temperature, pressure, kinetic mechanism and residence time in the reactor. The particles differ in equivalence ratio: the minimal $\phi_{min} = 0.4$ and maximal $\phi_{max} = 2.0$ (to include the flammability limits). The PSR equations are solved for each ϕ - the resulting mass fraction vector and temperature are then the $\overrightarrow{y_{ignition}}$ and T of the product particle. The example of the table is presented in the Tab 3.1.

Table 3.1: Example of an ignition cloud

No.	ϕ [-]	Hp [kJ]	Temperature [K]	mp [kg]	$\overrightarrow{y_p}$
1	0.4000	3575	1614.4	0.001	$\overrightarrow{y_{ignition}}(\phi = 0.4000)$
2	0.4020	3570	1619.3	0.001	$\overrightarrow{y_{ignition}}(\phi = 0.4020)$
...					

The procedure of assigning product particles from the table to the particle in the PSR is following. First, the equivalence ratio ϕ_p of the simulated particle is computed. If it does not lay between the ϕ_{min} and ϕ_{max} the particle remains unchanged - it is outside the combustibility limits (see the left scheme in the 3.4).

If ϕ_p is between ϕ_{min} and ϕ_{max} - the closest $\phi_{ignition}$ from the table is found. Then only the $\overrightarrow{y_p^{unreacted}}$ is overwritten with $\overrightarrow{y_{ignition}}$ (right scheme in the 3.4). The other properties: mass, mixture fraction and enthalpy remain unchanged.

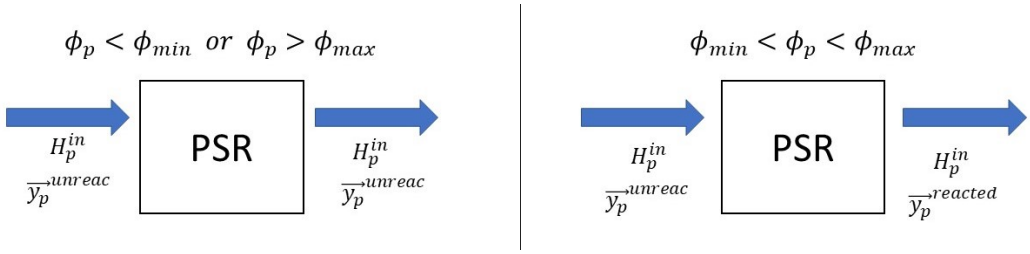

Figure 3.4: Change of particle properties depending on the ϕ_p

In the PFR all reactions are computed for each particle, with no use of tabular chemistry.

3.3 ACE Model

ACE (Advanced Combustion system for high Efficiency) is a staged, can combustor system. The Fig. 3.5 is showing the ACE position in the Siemens Energy gas turbine.

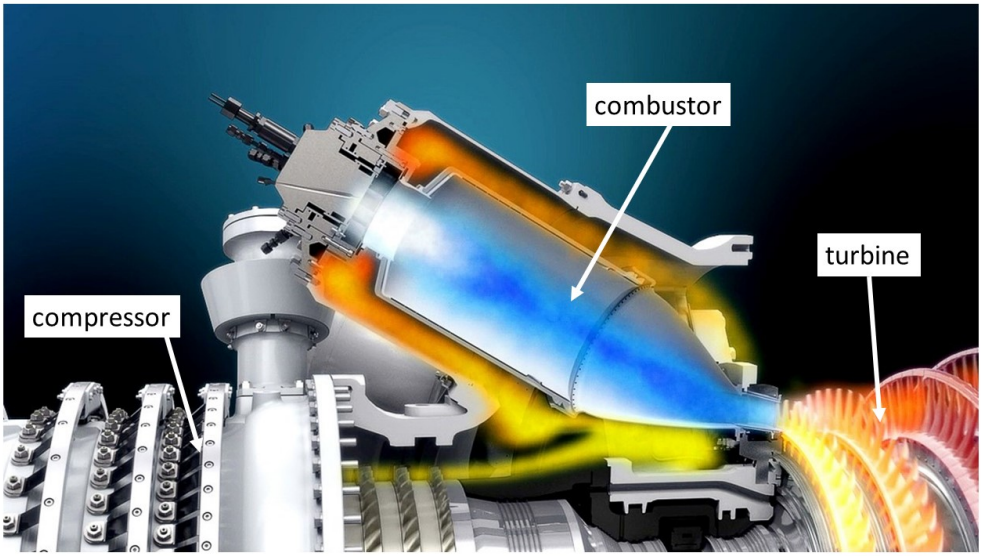

Figure 3.5: Combustor position in the Siemens Energy gas turbine; source - Siemens Energy offerings website [18].

ACE is equipped with two rings of premixed jets, placed around the pilot burner. Assuming axial symmetry, the upstream cross section area of the combustor was divided into 3 reaction zones: outer *stage B*, inner *stage A* and pilot flame - *stage P* (see the Figure 3.6). Then another, axial *stage X* is placed downstream of those three.
Downstream of the X stage the flows from different zones are merged together (Fig 3.6 and 3.8).

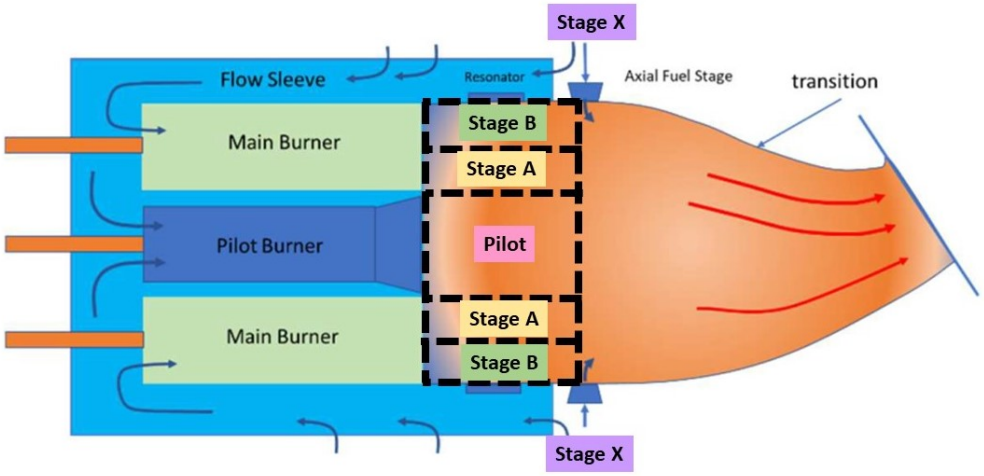

Figure 3.6: ACE scheme divided into stages: A, B, X and the Pilot.

The areas of each zone with respect to the total area A (see Fig. 3.7) are:

- $A_{pilot} = 0.07 \cdot A$
- $A_A = 0.37 \cdot A$
- $A_B = 0.56 \cdot A$

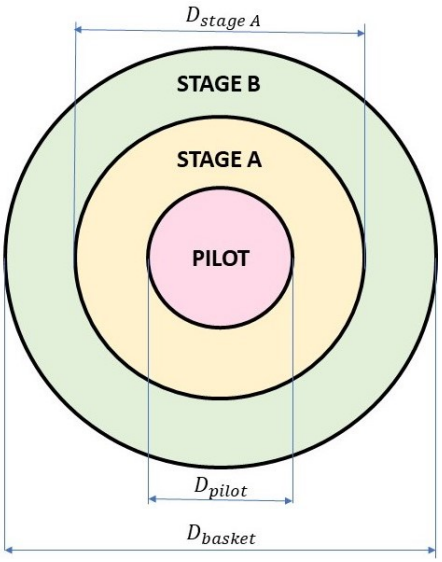

Figure 3.7: The division of the cross-sectional area into stages A, B and the Pilot.

The scheme of ACE model is presented in the Figure 3.8. As the combustor is axisymmetric, only half of the longitudinal section is shown. The elements of the model are described in the following sections (3.3.1 - 3.3.3).

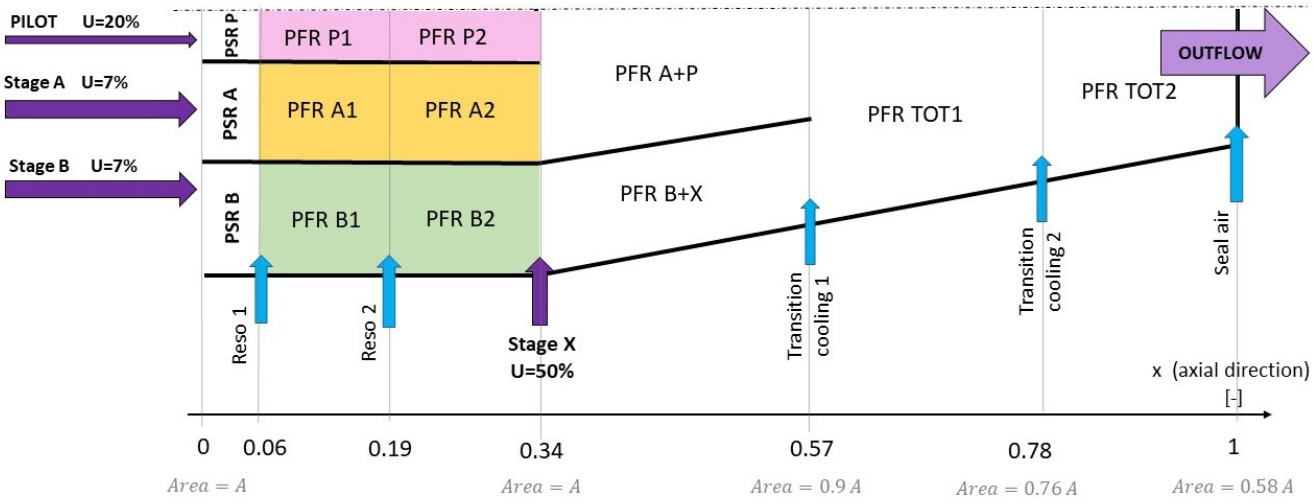

Figure 3.8: Model of the ACE. The axial dimension is scaled to non-dimensional value x=(0,1). Cross section areas are presented as fractions of the initial area A.

3.3.1 Inlets

All three zones are starting from the separate inlet elements with specified mass flows, thermodynamic conditions and the desired unmixedness in the flame front (since the next element is PSR).
Inlets are also placed downstream of the flame - to represent additional air streams and axial staging. In Fig. 3.8 inlet elements are depicted by arrows: blue for air streams and violet for air and fuel mixture.

3.3.2 PSR

The first elements connected to three respective inlets (A, B, pilot) are PSRs. It is where the flame front is simulated.

3.3.3 PFR

After ignition in the PSRs, the downstream combustion is modelled in the respective PFRs. The division into three zones (A, B, P) is continued until the $x = 0.34$.
It is done for two reasons. Firstly, the outer jets are mixed with air from the Helmholtz resonators (sets of cavities with necks placed to suppress pressure pulsations - *Reso 1* and *Reso 2* [4]). It is more physical to initially mix stage B with air (*PFR B1* and *PFR B2*) and then merge it with flow from the inner ring. Secondly, this division allows to simulate the pilot (*PFR P1, PFR P2* - higher equivalence ratio flow of high unmixedness

(20%)) before it mixes with the flow from the stages A and P. The division of *B stage* PFR is compulsory due to the resonator air flow at $x = 0.19$. Any additional air flow requires a merger element before placing a new reactor.
In case of stages A and P the division into two reactors (*PFR A1* and *PFR A2*, *PFR P1* and *PFR P2*) is made to improve the accuracy of the model: as each reactor initially mixes the flow and then proceeds with reactions, more reactors might mitigate the error caused by discretization. At the same time more reactors increase the computational time, so the stages A and B were divided into only two same-sized parts.
At $x = 0.34$ there is an additional stage introduced - *stage X*. It is a flow of fuel and air mixture with relatively high unmixedness ($> U = 50\%$) Again, firstly it is merged only with the outer flow (*stage B - PFR B+X*), whereas at this point *stage A* and pilot are already merged together (*PFR A+P*). Then from $x = 0.57$, after the transition air cooling is added, all flows proceed in the mutual reactors - *PFR TOT1* and *PFR TOT2*. Further burnt mixture leaves the combustor and enters the turbine.

The concept of dividing the combustor into mentioned reaction zones was then transferred to GeneAC. As later two settings of the X stage were examined (with and without X stage flow), two models: with and without the axial staging were created. Both are shown in the Appendix B.

3.4 Sensitivity Analysis

Most of the inputs of the model were taken from the experimental setup (such as air and fuel mass flows, thermodynamic conditions, inlet unmixedness). The model specific parameters: reactor mixing time scales, PSR residence time or chemical kinetics mechanism had to be selected. Therefore the sensitivity analysis of the ACE model for mentioned parameters (including the unmixedness) was carried out.

3.4.1 Chemical Mechanism Evaluation

Five potential reaction mechanisms that compute NOx were investigated: GRI3.0, GRI3.0 with Turanyi's modifications, NUIG 30, NUIG59 and NUIG120 (NUIG stands for the mechanisms developed in cooperation of Siemens Energy and University of Galway; still in progress). The first two consist of the same 53 species. They differ only in several rate coefficients (see 2.6.4). The NUIG mechanisms are reduced versions of the full combustion mechanism and have respectively: 30, 59 and 120 species.

The impact of the mechanism was examined using a simple system consisting of a single inlet, PSR ($\tau_{res} = 10ms$) and the outlet. The combustion was simulated for different equivalence ratios from 0.37 to 2.0 for two different pressure levels: $1bar$ (Fig. 3.9) and $20bar$ (Fig. 3.10). Fuel and oxidizer mixture was assumed to be perfectly mixed.

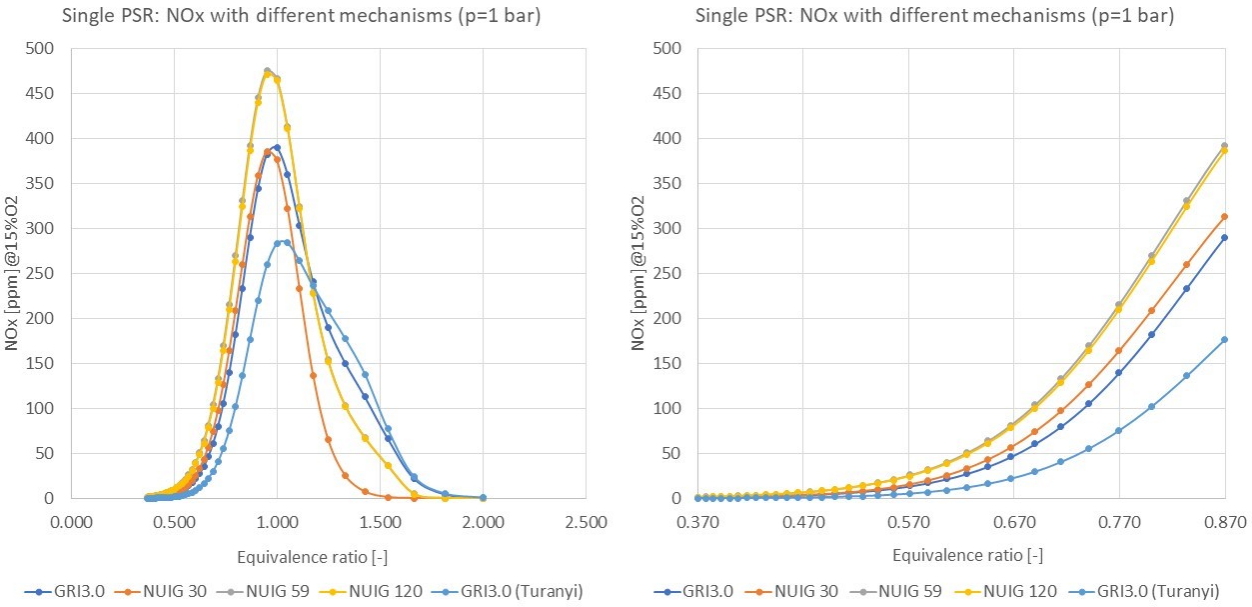

Figure 3.9: NOx vs. equivalence ratio for different mechanisms at $1bar$, left plot: $\phi \in (0.37, 2.0)$, right plot: zoomed in $\phi \in (0.37, 0.87)$

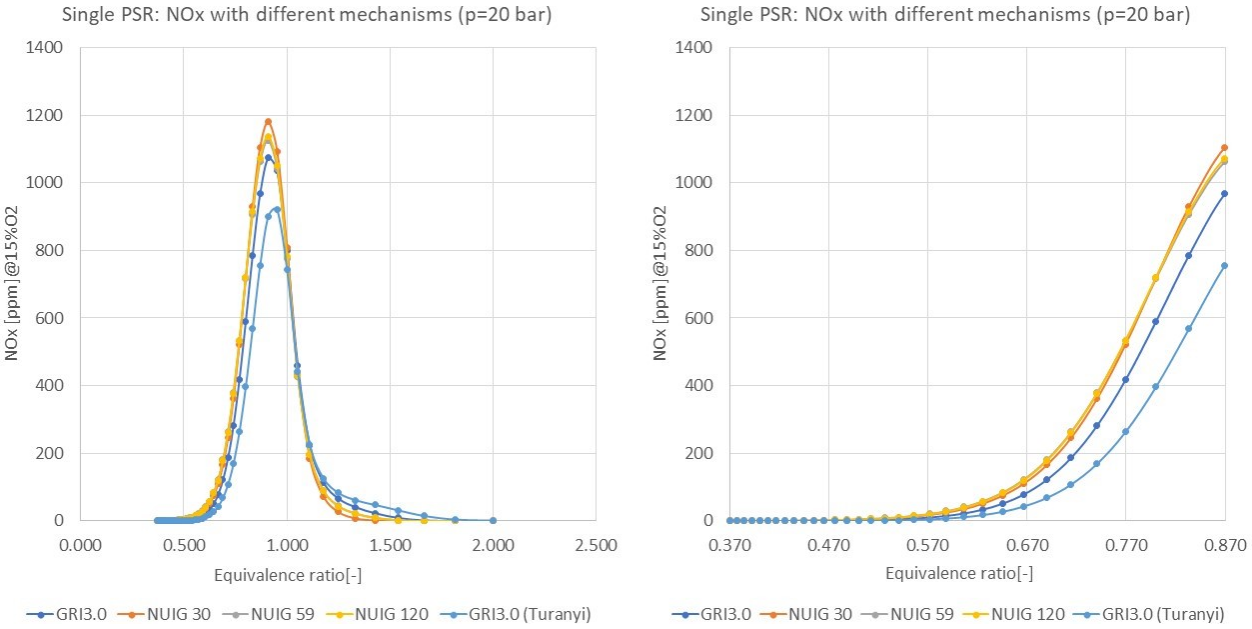

Figure 3.10: NOx vs. equivalence ratio for different mechanisms at $20bar$, left plot: $\phi \in (0.37, 2.0)$, right plot: zoomed in $\phi \in (0.37, 0.87)$

For $p = 1bar$ NUIG59 and NUIG120 are characterised with highest NOx. GRI3.0 and NUIG30 present similar results (especially in the lean area). GRI3.0 with Turanyi's modifications produces the lowest NOx. Another interesting observation is that the maximum of the Turanyi's emissions are displaced in the richer direction with respect to the other mechanisms.

For $p = 20bar$ the difference in NOx emissions between the mechanisms is smaller than for $p = 1bar$. At higher pressure it is the NUIG30, that has the highest NOx peak. The other Galway-based mechanisms produce little less NOx. GRI3.0's result is lower, and again the modified GRI3.0 shows the lowest NOx production.

In conclusion, there are clear differences between the mechanisms. It was desired to proceed with at least one of NUIG mechanisms (since their results are similar), GRI3.0 and the modified GRI3.0. The largest problem with NUIG mechanisms was the computational time, that was five times longer than for the other ones. Since the time for simulations was limited and the NUIG results were not far from the GRI3.0 (so we do not expect large differences between each other) - Galway mechanisms had to be left out. Only GRI3.0 and modified GRI3.0 were proceeded with.

3.4.2 Design of Experiment

Further sensitivity analysis was done for the full ACE model without axial staging. The Table 3.2 presents parameters examined in the sensitivity analysis and their values.

Table 3.2: Parameters of the sensitivity analysis

Property	**Values investigated**
Chemical kinetics mechanism	GRI 3.0, GRI 3.0 with Turanyi modifications
τ_{mixPFR}	3ms, 5ms, 7ms
τ_{mixPSR}	1ms, 2ms, 3ms
τ_{resPSR}	0.15ms, 0.7ms, 1.3ms
$U_A = U_B$	5%, 10%, 15%

Since the computational time of a combustor simulation ($\approx 4h$) does not allow to run the full factorial of the properties ($3^4 \cdot 2 = 162$), the sets of inputs were chosen with help of Design of Experiment method. Using Plackett-Burman Design the number of runs was reduced to 13 for each mechanism ($2 \cdot 13 = 26$ in total, see Appendix A). The results of the screening design are presented on the Pareto chart - comprising of absolute values of the standardized effects (Fig. 3.11). The red reference line at $Standarised\ Effect = 2.086$ indicates which factors are statistically significant.

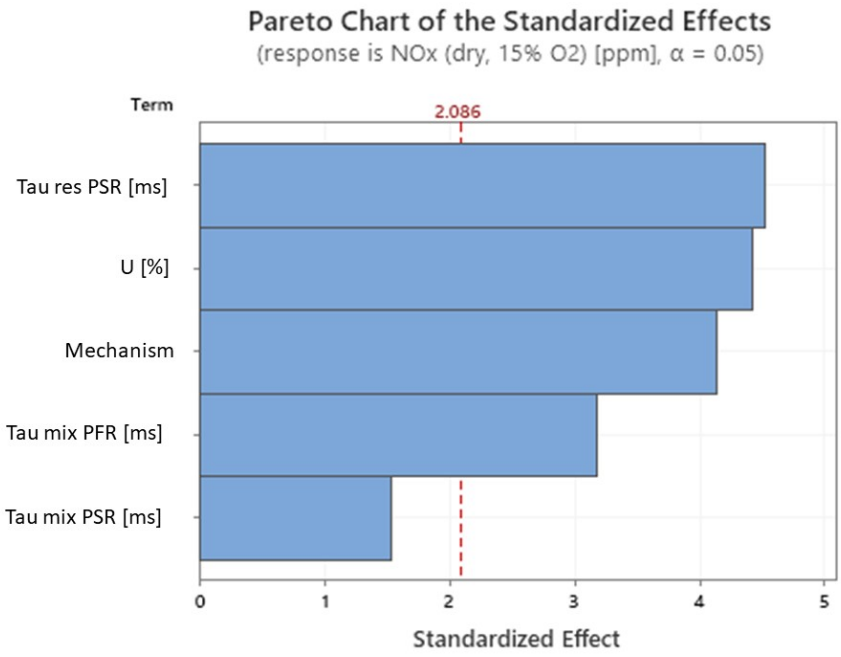

Figure 3.11: Pareto chart for the examined parameters

In this case the only insignificant parameter is the mixing time scale in the PSR. This behaviour is expected, since the PSR residence time is relatively small ($\tau_{res} \in (0.15, 1.3)\, ms$ with respect to the $\tau_{mix} \in (1, 3)\, ms$). Hence mixing in the PSR is limited.

The regression equation in uncoded units obtained from screening the Plackett-Burman Design is:

$$\begin{aligned} NOx(dry, 15\%O_2)[ppm] = 9.9 + 6.55 \cdot \tau_{mix,PSR}[ms] + 6.75 \cdot \tau_{mix,PFR}[ms] + \\ +3.758 \cdot U[\%] - 33.42 \cdot \tau_{res,PSR}[ms] + 16.91 \cdot M \end{aligned} \tag{3.16}$$

The M factor stands for the Mechanism. It is $M = 1$ for GRI3.0 and $M = 0$ for Turanyi. As one can see from the equation, the strong effect of the parameters is following:

- $U_A = U_B$ - the higher the unmixedness, the higher the NOx (positive regression coefficient 3.758)
- *Mechanism* - change from Turanyi to GRI3.0 increases the emissions by around 17ppm (positive regression coefficient ≈ 17)
- $\tau_{mix,PFR}$, $\tau_{mix,PSR}$ - with worse mixing (higher mixing time scale) the NOx is increasing (positive coefficients 6.55 and 6.75). Despite the similar regression coefficients, the impact is way larger in case of PFR - it is due to the larger mixing time scales in this reactor.

- Increase of the residence time in the PSR results in decrease in NOx (negative coefficient equal to -33.42). It might be due to the way mixing and reactions are ordered in the reactor. As mixing (computed using τ_{res} and τ_{mix}) happens in the very beginning, larger residence time causes large drop of unmixedness before the ignition.

3.4.3 Monte Carlo Validation

To check if Monte Carlo tool produces trustworthy results, a method validation was carried out: the perfectly mixed result (general GeneAC) was compared to the Monte Carlo ($U = 0\%$ and all $\tau_{mix} = 10^{-10}s$). The simulation was run for a full combustor model (with X stage), using GRI3.0 mechanism. The results are presented in Table 3.3.

Table 3.3: Monte Carlo Tool Validation

	Perfectly mixed	Monte Carlo $U = 0$	Monte Carlo $U \neq 0$
NOx (dry, 15%O_2) [ppm]	32.05	32.45	37.10

The deviation of 0% Monte Carlo from perfectly mixed case was below $0.5ppm$. In comparison to $5ppm$ difference (between $U \neq 0$ and perfectly mixed) this deviation was considered negligible.

3.4.4 Number of Particles

Another parameter necessary to simulate the model is the number of particles. Obviously, the more particles, the higher is accuracy of a pdf shape. On the other hand large number of particles increases the computational time of the simulation.

To check if the default mass of particle ($1g$) ensures desired accuracy, simulations of the same test case with different number of particles were run (Table 3.4).

Table 3.4: Number of particles impact on NOx (dry, 15%O_2)

No. of Particles	Particle mass [g]	**NOx Monte Carlo (dry, 15%O2) [ppm]**
14 225	2	43.94
28 450	1	43.94
56 900	0.5	43.96

The results computed for different number of particles did not show large differences, so it was decided to proceed with the default particle mass equal to $1g$.

3.5 Parameters Selection

After identifying the impact of parameters, the final choice of the parameters was made.

3.5.1 PSR residence time

The flame is modelled in the PSR. As the PSR residence time should be equal to the flame residence time, the flame CFD results were consulted. The mean flame residence time was found to be $\tau_{flame} = 0.2ms$ - the time computed from the average distance between non-reacted and fully reacted mixture. Unfortunately this time was to short to ensure ignition in the flammability limits ($\phi \in (0.4, 2.0)$). As ignition of all the particles from that interval was a priority, the smallest residence time satisfying this condition was taken: $\tau_{res,PSR} = 0.7ms$. The expected effect of this modification is an increase of NOx emissions (since the residence time with high unmixedness is larger), but it is necessary for the successful combustion simulation.

3.5.2 PSR mixing time scale

Mixing in all PSRs is disabled ($\tau_{mixPSR} = 1000ms$), since the inlet mixture fraction pdfs are already the desired mean flame front distributions. The flow starts mixing after being ignited, in the PFR.

3.5.3 PFR mixing time scale

The mixing time scale in the postflame region was deduced from CFD $\frac{k}{\epsilon}$ distribution in the combustor. The $\frac{k}{\epsilon}$ values on the contour plot downstream of the flame laid between 1 and $2ms$. The lower value was chosen: $\tau_{mix,PFR} = 1ms$.

3.5.4 Mixture fraction pdf in the inlet

The unmixedness in the premixer outlet was taken as a value from CFD results (fixed for each kind of premixer). In cases examined in the thesis the unmixedness values were: for stages A and B: $U_A = U_B = 7\%$, for the pilot: $U_P = 20\%$ and for stage X $U_X = 50\%$ (see 3.8). The inlet mixture fraction pdfs for stage A, B, P and X are presented in the Figure 3.12.

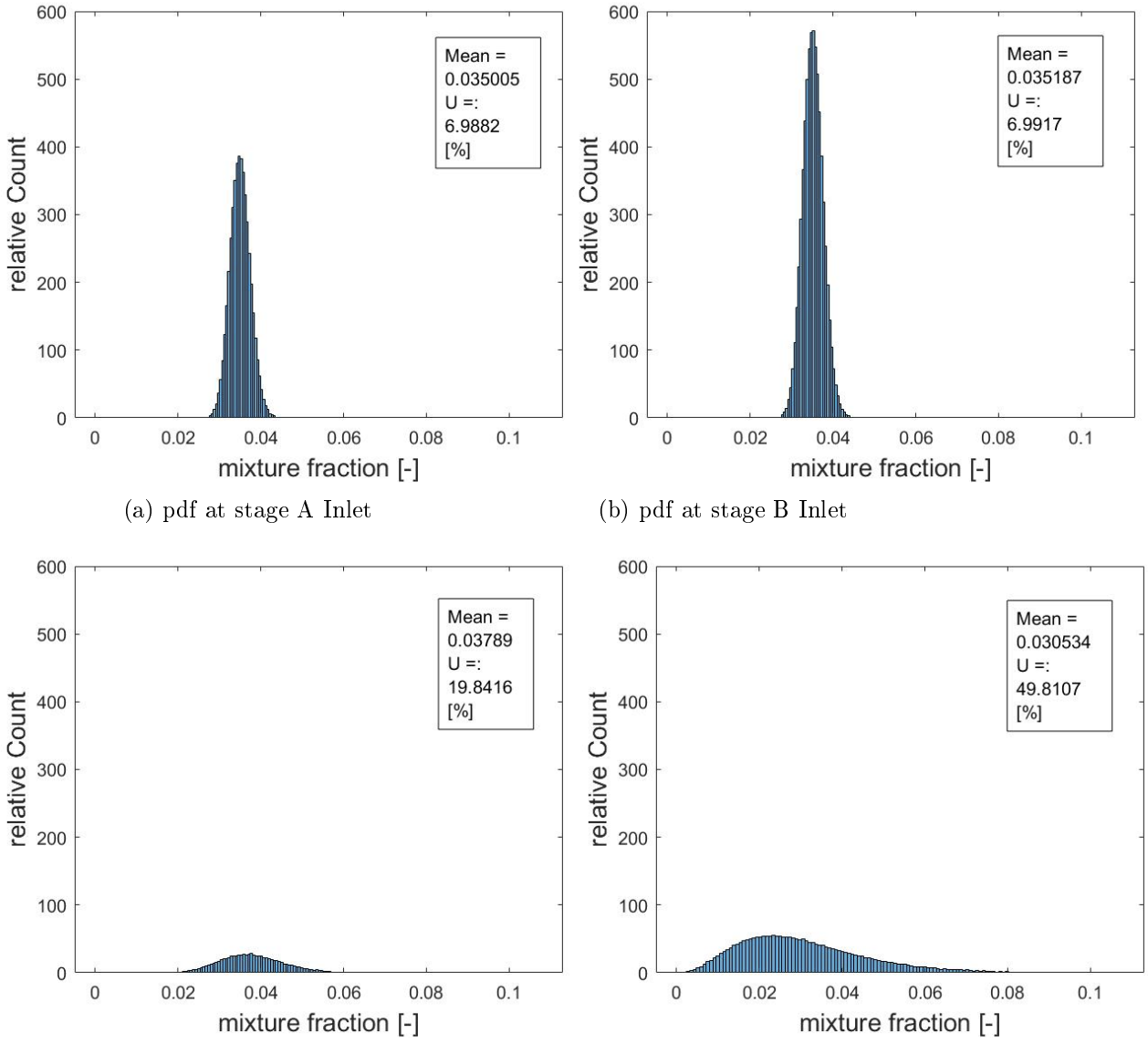

(a) pdf at stage A Inlet

(b) pdf at stage B Inlet

(c) pdf at stage P Inlet

(d) pdf at stage X Inlet

Figure 3.12: Prescribed pdfs in the mixture inlets

3.5.5 Chemical Kinetics Mechanism

As sensitivity analysis has shown the mechanism to have a largest impact, the combustion was simulated with both available mechanisms: GRI3.0 and GRI3.0 with Turanyi modifications.

Chapter 4

Results and Comparison with Experimental Data

To validate the combustor model, the results of the simulations were compared to the available experimental data.
The experiments were carried out in the Siemens Energy test centre in Berlin Area. The company was testing the combustor with different boundary conditions. The geometry and residence time in the combustor did not differ between the specimens. Among multiple test the 16 cases were chosen and reproduced using the GeneAC model.

4.1 Experimental data

The boundary conditions of the simulations were taken from the experimental cases.
The factors differentiating the test cases were: ϕ, pressure level and different pilot fractions: ratios of fuel fed into the pilot to the total fuel flow in stages A, B and P - $PMP = \frac{\dot{m}_{fuel,pilot}}{\dot{m}_{fuel,A}+\dot{m}_{fuel,B}+\dot{m}_{fuel,pilot}}$.

Another difference between the examined cases was presence of the stage X - an additional stage downstream of the flame. It is used to reduce NOx emissions by shortening the residence time in the combustor for part of the mixture.
The mass flows in the stage X is zero for closed ($\dot{m}_X = 0$) and non-zero for open ($\dot{m}_X \neq 0$).

All altered properties are presented in the Table 4.1.

Table 4.1: Altered parameters of the experiments

Property	**Values investigated**
Pressure level	$8bar$, $16bar$
ϕ	between 0.5 and 0.6
PMP	5%, 6%, 7%, 7.5%
X stage	not active, active

4.2 Input data sanity check

To ensure the input data was set correctly and the tool obeys basic rules of combustion, the sanity check was done. The combustor outlet temperature vs. equivalence ratio dependency was plotted (see Fig. 4.1). The aim was obtaining graph similar to Fig. 2.2. In the range of equivalence ratios tested in the combustor $\phi \in (0.5, 0.6)$ the temperature vs. ϕ curve should be a straight line, same for with and without the X stage active.

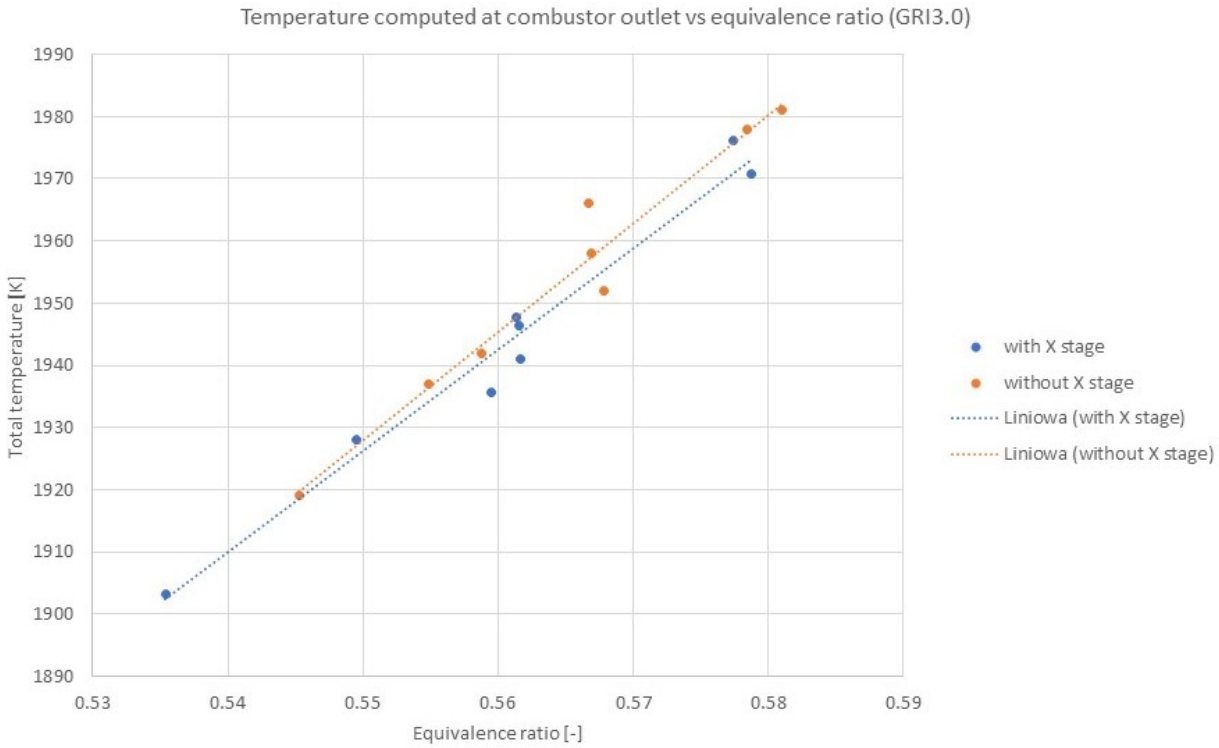

Figure 4.1: Temperature vs. equivalence ratio dependence for all the test cases.

As expected, test points almost form a straight line. Small deviations from the line might be caused by the mass flow uncertainties.

4.2.1 ACE without X Stage

The table with results for $\dot{m}_X = 0$ is presented in 4.2. For data protection all the NOx emissions were scaled - divided by the maximal NOx in $[ppm]$ value of all 16 test cases. The $U = 0\%$ column stands for simulation of perfectly mixed flow, while $U \neq 0\%$ is the Monte Carlo result.

Table 4.2: Results for the non-X-stage cases

No.	p [*bar*]	ϕ [-]	PMP [%]	NOx scaled [-]				
				GRI3.0		Turanyi		Exper.
				$U = 0$	$U \neq 0$	$U = 0$	$U \neq 0$	
1	8	0.568	7.5	0.60	0.72	0.30	0.39	0.59
2		0.567	5	0.55	0.63	0.27	0.32	0.38
3		0.581	5	0.73	0.83	0.37	0.43	0.53
4		0.545	5	0.37	0.42	0.17	0.21	0.24
5	16	0.559	7	0.58	0.70	0.29	0.38	0.76
6		0.555	5	0.54	0.61	0.27	0.32	0.48
7		0.567	5	0.69	0.79	0.36	0.42	0.63
8		0.578	5	0.87	1.00	0.46	0.54	0.84

The first observation is, that the Monte Carlo cases always present higher NOx than the perfectly mixed ones. This behaviour is expected, since in the Monte Carlo simulation we deal with non-zero unmixedness. Another remark is, that for the cases computed using GRI3.0, emissions are always higher than the Turanyi ones. In most of the GRI3.0 cases the NOx is overshooting the experimental, while for Turanyi the computed values are below the test ones.

4.2.2 ACE with X stage

The table with results for $\dot{m}_X \neq 0$ is presented in 4.3. Again, all the NOx emissions were scaled - divided by the maximal NOx in [*ppm*] value of all 16 test cases. As in the non-X-stage table $U = 0\%$ column stands for simulation of perfectly mixed flow, while $U \neq 0\%$ is the Monte Carlo result.

Table 4.3: Results for the X-stage cases

No.	p	fi [-]	PMP [%]	NOx scaled [-]				
				GRI3.0		Turanyi		Exper.
				$U = 0$	$U \neq 0$	$U = 0$	$U \neq 0$	
1	8	0.559	5	0.43	0.50	0.21	0.25	0.27
2		0.562	7	0.45	0.54	0.22	0.28	0.36
3		0.562	5	0.47	0.53	0.23	0.27	0.30
4		0.579	5	0.63	0.71	0.32	0.37	0.42
5	16	0.561	5	0.57	0.66	0.29	0.35	0.48
6		0.535	6	0.31	0.37	0.16	0.19	0.30
7		0.577	5	0.80	0.92	0.42	0.49	0.64
8		0.550	5	0.45	0.52	0.23	0.27	0.36

The behaviour of NOx concentration for cases with X stage does not differ from the

ones without the axial stage: results considering non-zero unmixedness are higher than the perfectly mixed. Also the mechanism has the same impact: GRI3.0 is overshooting the test NOx values, while Turanyi's results are smaller than experimental.

4.3 Impact of the Test Parameters

Figure 4.2 presents the dependence of NOx emissions (scaled) on the equivalence ratio for 4 different settings: top left - $p = 8bar$ and no X stage, top right - $p = 8bar$ with X stage, bottom left - $p = 16bar$ and no X stage, bottom right - $p = 16bar$ with axial staging.
Data points constructing the exponential trend lines are for $PMP = 5\%$. The higher pilot fractions PMP^* are represented by red markers.
The qualitative impact of the test parameters: equivalence ratio, pressure, axial staging and pilot fraction is described below.

Equivalence Ratio

The NOx emissions are exponentially dependent on the equivalence ratio. For $PMP = 5\%$ both experimental and computational results form exponential curves - NOx is strongly dependent on ϕ. This behaviour was expected, due to large influence of the temperature on thermal NOx emissions (see Fig. 2.12 and 4.1).

Pilot Fraction

For experimental values larger PMP results in higher NOx. This effect is more visible in cases without axial staging - where pilot has more impact on the emissions.
Higher pilot fraction resulting in higher NOx is only slightly visible with the computational results - the distance between points with PMP^* and the exponential trend lines of $PMP = 5\%$ is smaller than for the experiments. It means that the model is not sensitive enough to fully resolve the effect of different pilot fractions.

Axial staging

As expected, the NOx emissions are reduced with axial staging, i.e. shortening the residence time for part of the fuel-air mixture.
The quantitative description of the reduction is presented in section 4.4.

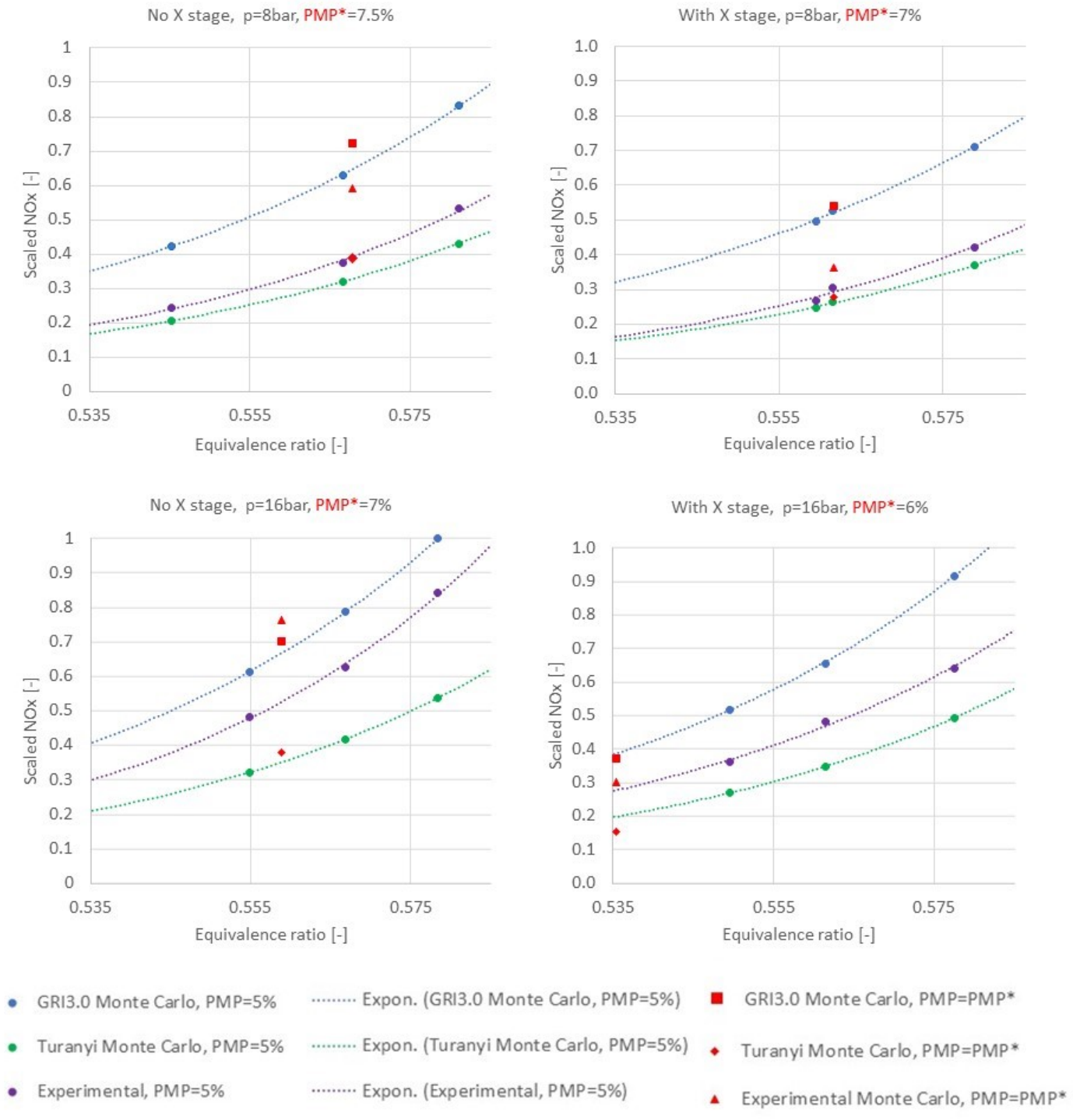

Figure 4.2: Scaled NOx vs. equivalence ratio for cases without the X stage (left plots) and with X stage (right plots). Upper plots have $p = 8bar$, for lower ones $p = 16bar$

Pressure

As one can see, higher pressure results in higher NOx. Also the quality of prediction changes with pressure: in case of $p = 8bar$ Turanyi is closer to the experimental data than at higher pressure. For GRI3.0 simulations at $p = 16bar$ the difference between the simulation and experiments is smaller than at $8bar$.
The quantitative dependence of $NOx(p)$ is treated in section 4.5.

4.4 Axial Staging Effect

To check if the model's response to axial staging is the same as in the experiment, the exponential curves (test points trend-lines) were compared - see the Fig. 4.3.

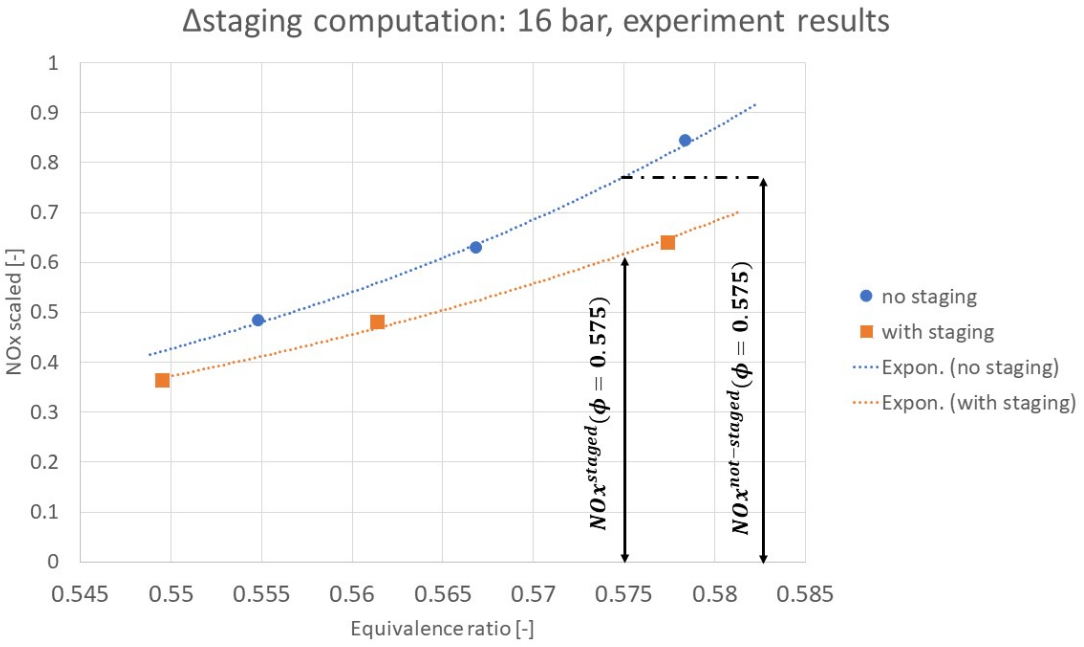

Figure 4.3: Comparison of two exponential curves: with and without axial staging.

The reduction of NOx with respect to value without axial staging was computed as:

$$\Delta_{staging} = \frac{NOx^{not-staged} - NOx^{staged}}{NOx^{not-staged}} \tag{4.1}$$

Where NOx^{staged} and $NOx^{not-staged}$ are scaled mole fractions of dry $15\%O_2$ NOx $[ppm]$ for combustor with and without staged combustion respectively. NOx^{staged} and $NOx^{not-staged}$ for $\phi = 0.575$ are marked in the figure 4.3.

This procedure was repeated for ϕ values between 0.555 and 0.585, for experiments and both kinetic mechanisms simulations. The reduction of NOx due to axial staging for two pressure levels is plotted in Fig. 4.4.

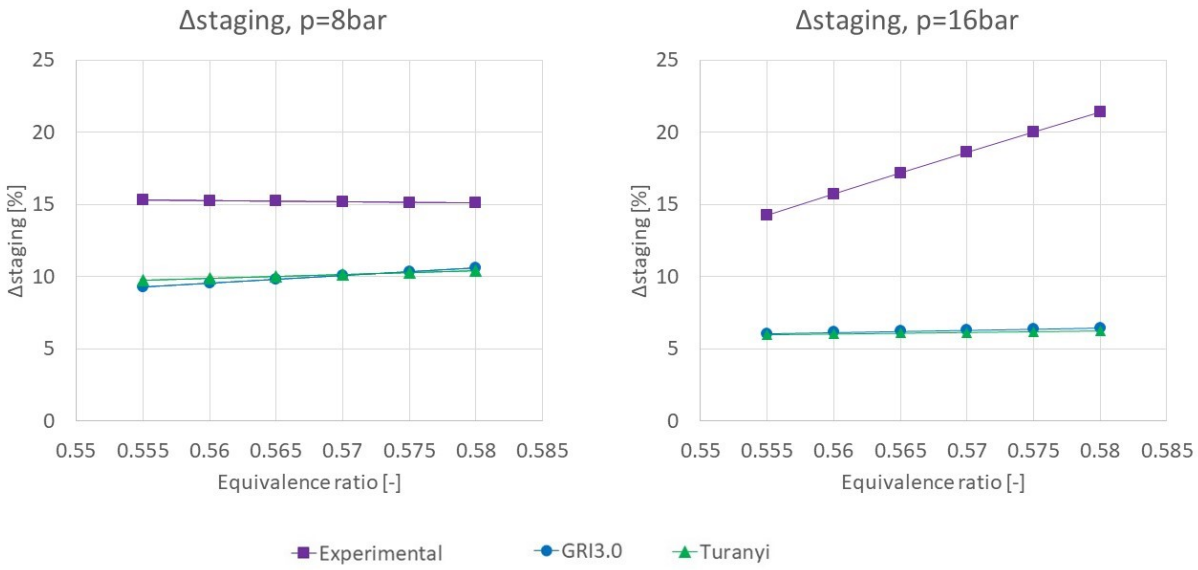

Figure 4.4: $\Delta_{staging}$ vs. ϕ for experiment and simulations. Left plot - $p = 8bar$, right plot - $p = 16bar$.

The experimental $\Delta_{staging}$ is showing interesting behaviour: at $8bar$ the NOx reduction is constant for all ϕ, while at $p = 16bar$ the reduction is increasing linearly with ϕ. What is also visible, the simulation $\Delta_{staging}$ is the same for both kinetic mechanisms - difference between Turanyi and GRI3.0 is almost invisible. Moreover, in case of simulation results, the $\Delta_{staging}$ stays constant at both pressure levels - increase of $\Delta_{staging}$ is not visible in the simulations results.
The simulated reduction of NOx was smaller than in the experiments for both pressure levels - for $p = 8bar$ the reduction was 30% lesser. In case of $p = 16bar$ the difference between experiments and simulations was even larger.

4.5 Pressure dependence

As experiments and simulations were carried out at two pressure levels, the pressure dependence of NOx could be examined. Assuming $NOx(\phi, p) \approx g(\phi) \cdot p^{\xi}$ and basing on interpolated plots of NOx vs. ϕ, the power ξ was computed. This procedure was followed for experimental results, GRI3.0 and Turanyi computations for different ϕ values (see Fig. 4.5).

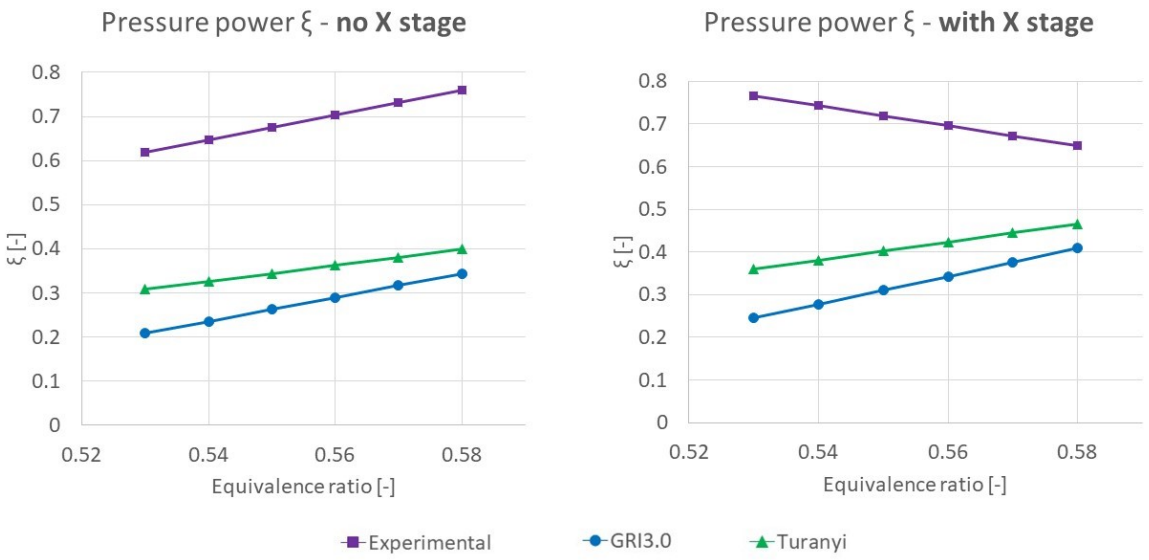

Figure 4.5: ξ vs. ϕ for experiment and simulations. On the left combustion without the X stage, on the right with X stage.

First thing one can see, is that there is no single pressure dependence. The ξ is changing with equivalence ratio linearly (for $\phi \in (0.53, 0.58)$). In both plots (with and without axial staging) the pressure impact is under-predicted by the model (with Turanyi performing slightly better).
Without axial staging the trend of $\xi(\phi)$ is the same for experiments and simulations - pressure power is increasing with equivalence ratio.
The opposite thing is happening for the cases with axial staging - the experimental $\xi(\phi)$ is decreasing while the simulation values are increasing with ϕ. The reason for this behaviour might be the low accuracy exponential interpolation of NOx vs. ϕ (see Fig. 4.2). Three data points might not be enough to accurately predict the emissions for other ϕ.

4.6 NOx source

As discussed in the 2.6, the combustion NOx is being produced via three pathways: thermal, prompt and N_2O. To examine the contribution of each of those three, some changes were applied to the GRI3.0 mechanism. After simulating the combustor with the full mechanism, three mechanisms with only one pathway active (reaction rates of the others set to 0) were used. The reactions disabled in each altered mechanism are listed in Table 4.4.

Table 4.4: Reactions deactivated in each altered mechanism

Mechanism	GRI3.0_THERMAL	GRI3.0_PROMPT	GRI3.0_N2O
Reactions disabled	$N_2O + O \longrightarrow 2NO$ $CH_2 + N_2 \longrightarrow HCN + N$	$N_2O + O \longrightarrow 2NO$ $N_2 + O \longrightarrow NO + N$ $N + O_2 \longrightarrow NO + O$ $N + OH \longrightarrow NO + H$	$CH_2 + N_2 \longrightarrow HCN + N$ $N_2 + O \longrightarrow NO + N$ $N + O_2 \longrightarrow NO + O$ $N + OH \longrightarrow NO + H$

The combustion was simulated for two $16bar$ cases: with and without the X stage. The equivalence ratios for those cases are equal ($\phi = 0.578$) Results are presented in the Table 4.5.

Table 4.5: Different NOx pathway contributions

	NOx(of the mechanism)/ NOx(GRI3.0)		
Mechanism	**GRI3.0_THERMAL**	**GRI3.0_PROMPT**	**GRI3.0_N2O**
Case 8 without X stage	0.86	0.19	0.23
Case 7 with X stage	0.86	0.20	0.23

As the NOx produced via one pathway is also depending on the other ones, the entries for thermal, prompt and N_2O do not add up to 1.
In both cases (with and without the X stage) the contributions are similar. Majority of NOx is produced via thermal pathway, while prompt and N_2O present similar importance.

4.7 Mixture Fraction Histogram Evaluation

Besides looking at the NOx emissions, the quality of the mixing model was evaluated. To compare the GeneAC with CFD results, particle cloud mixture fraction histograms at different cross sections were extracted. The cross sections' positions are presented in the Fig. 4.6.

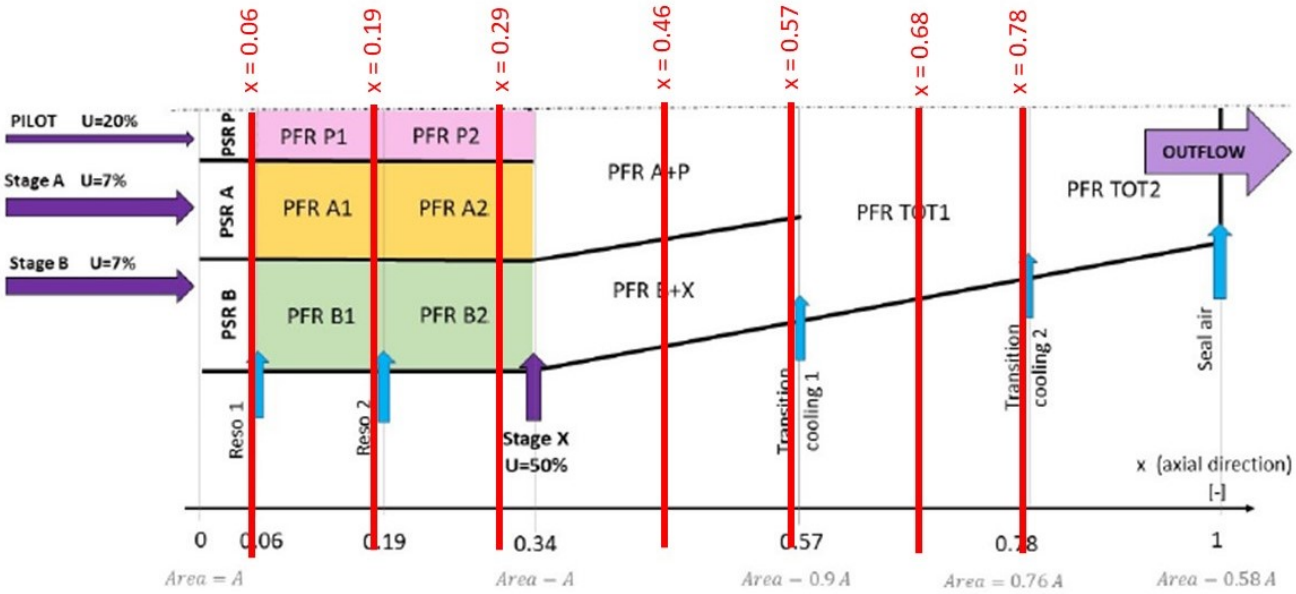

Figure 4.6: Cross sections with extracted mixture fraction histograms.

The histograms are presented in subsections 4.7.1 and 4.7.2. The plot reading tips are following:

- y-axis is labelled "relative Count". It stands for the number of particles (or control areas in CFD) that have mixture fraction laying between the bin edges.
- There are two overlapping histograms on each figure (see an example plot in Fig. 4.7). The light red histogram is the one from CFD. The blue one: GeneAC. When bars of both of them are overlapping, the resultant colour is darker red.

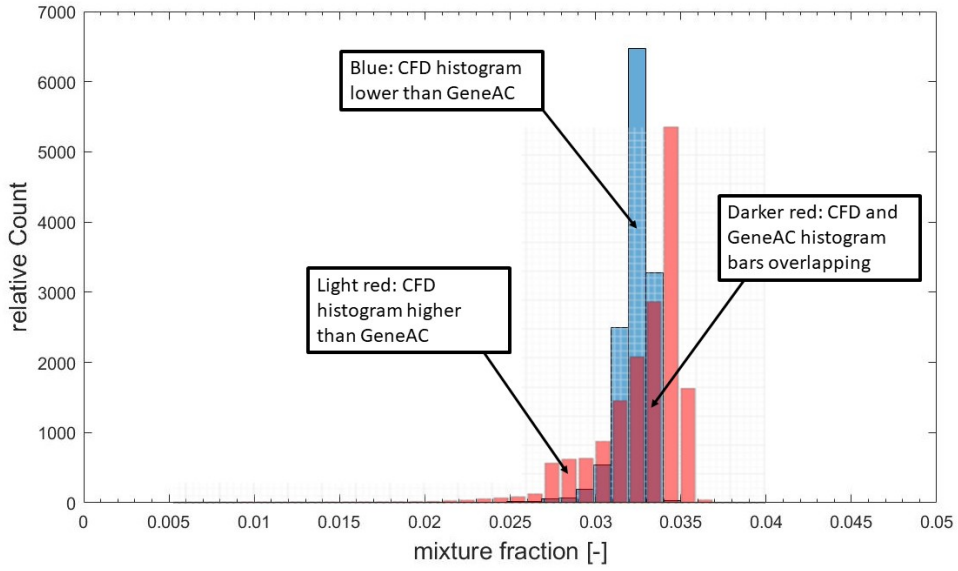

Figure 4.7: Legend

4.7.1 Upstream of the Axial Stage

The histograms (both CFD - red and GeneAC - blue) at different x positions (upstream of the axial stage) are presented in Fig. 4.8 - 4.10.

As one can see, shapes of the GeneAC histograms matched the CFD ones - peaks' positions were similar. The difference between them is the pdf width - the narrower distribution in GeneAC signalises that mixing efficiency is overestimated by the model. What is also worth mentioning, the CFD histogram at $x = 0.06$ (Fig. 4.8) has a long tail on the lean side (which has a strong impact on the unmixedness value). This is not resolved in GeneAC distribution.

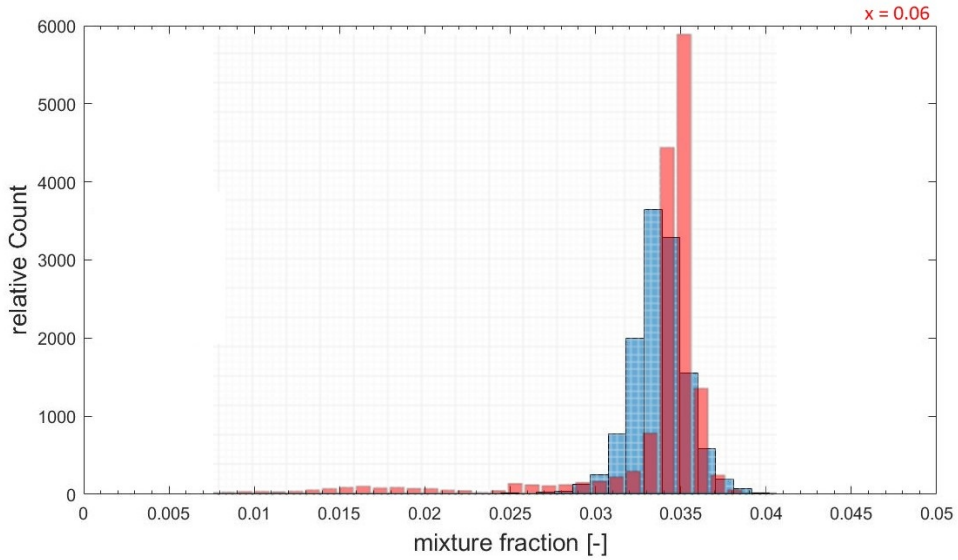

Figure 4.8: Mixture fraction histograms comparison at $x = 0.06$, CFD - red and GeneAC - blue.

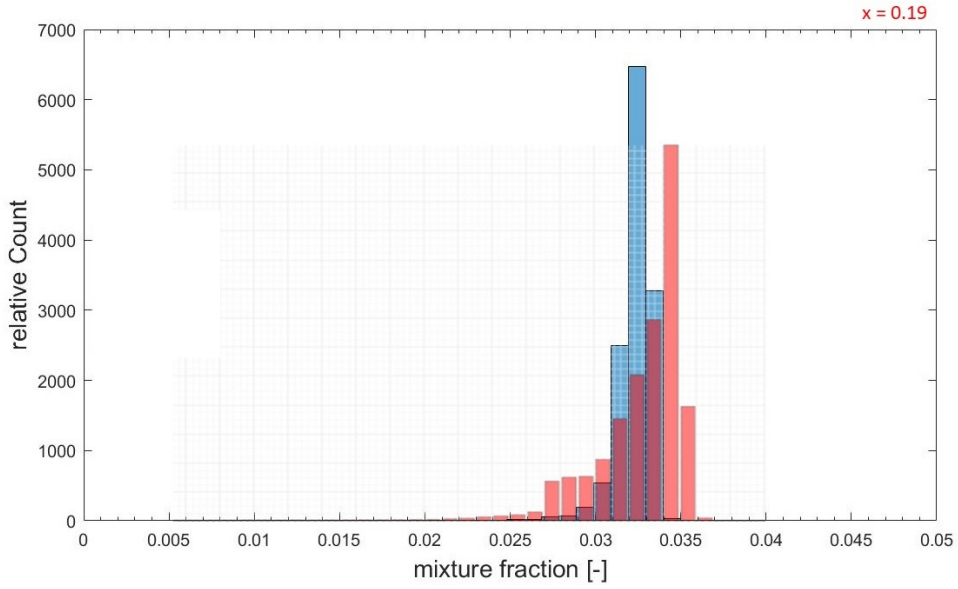

Figure 4.9: Mixture fraction histograms comparison at $x = 0.19$, CFD - red and GeneAC - blue.

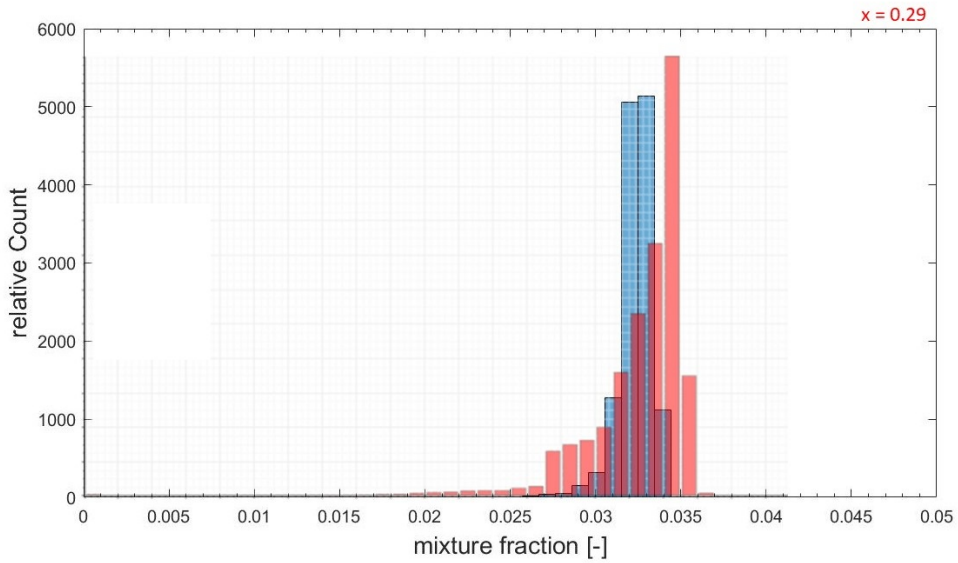

Figure 4.10: Mixture fraction histograms comparison at $x = 0.29$, CFD - red and GeneAC - blue.

4.7.2 Downstream of the Axial Stage

Initially, all the mixing time scales in all PFRs were equal to $1ms$. The values presented in sections 4.1 - 4.6 are computed with this setting.
During initial histogram evaluation, the mixing overestimation by the GeneAC was noticed (also downstream of the axial stage - see the left sides of Fig. 4.11 - 4.14). So another - worse mixing scenario was checked.
According to the k/ϵ plot mixing time scales in the combustor should lay between 1 and $2ms$. This time the higher limit of mentioned interval was investigated. The mixing time scales were increased only downstream of the X stage ($x = 0.34$), as this is the area we expect mixing to be less efficient than in the upstream zone. Therefore the downstream PFR τ_{mix} were changed from the previous $1ms$ to $\tau_{mix,downstream} = 2ms$.

As the change was applied only downstream, it was only the cross-sections at $x > 0.34$ to be affected. The mixture fraction histograms are presented for $x = \{0.46, 0.57, 0.68, 0.78\}$ positions (Fig. 4.11-4.14).

Although for the first examined cross-section ($x = 0.46$) histograms look similar, downstream the differences are more and more visible. Since the GeneAC histograms are wider for the $\tau_{mix,downstream} = 2ms$, the right hand side histograms ($2ms$) seem to be more consistent with CFD results than the left hand side ones ($1ms$).

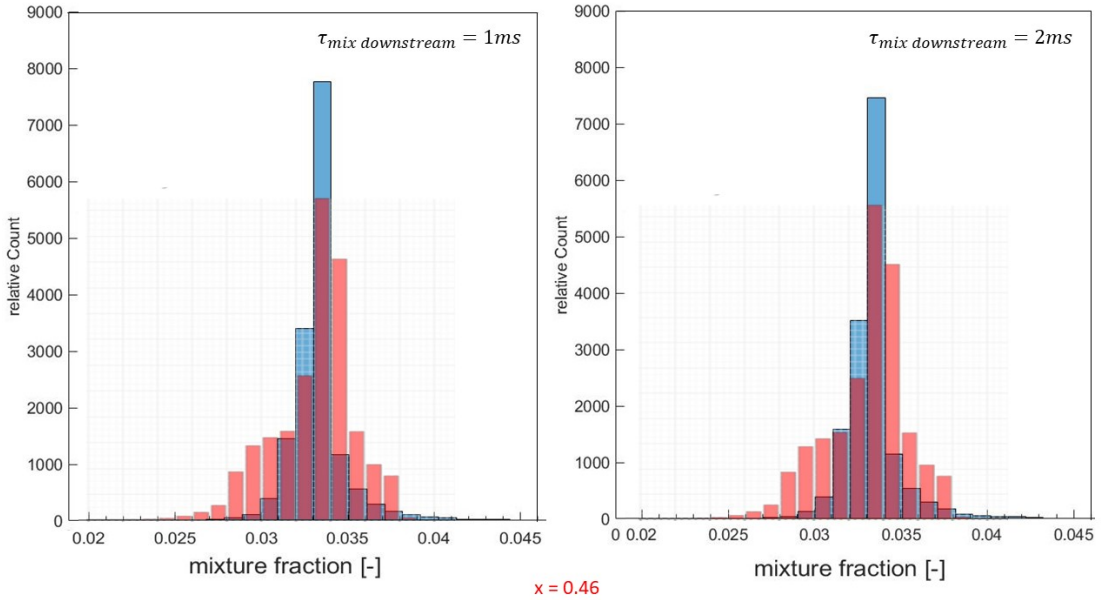

Figure 4.11: Mixture fraction histograms comparison at $x = 0.46$, CFD - red and GeneAC - blue. Left plot: $\tau_{mix,downstream} = 1ms$, right plot: $\tau_{mix,downstream} = 2ms$.

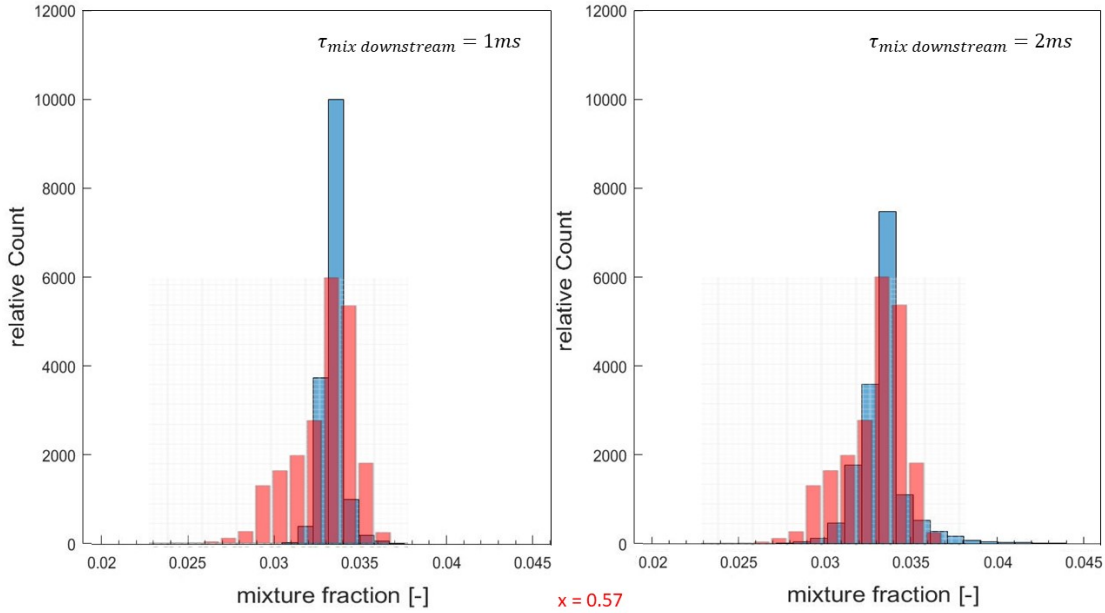

Figure 4.12: Mixture fraction histograms comparison at $x = 0.57$, CFD - red and GeneAC - blue. Left plot: $\tau_{mix,downstream} = 1ms$, right plot: $\tau_{mix,downstream} = 2ms$.

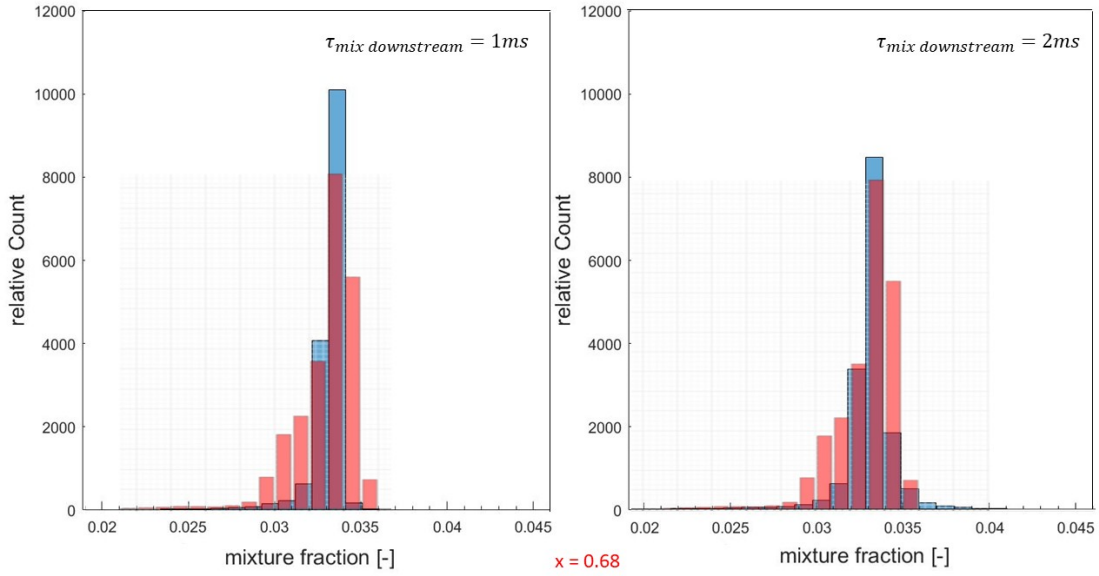

Figure 4.13: Mixture fraction histograms comparison at $x = 0.68$, CFD - red and GeneAC - blue. Left plot: $\tau_{mix,downstream} = 1ms$, right plot: $\tau_{mix,downstream} = 2ms$.

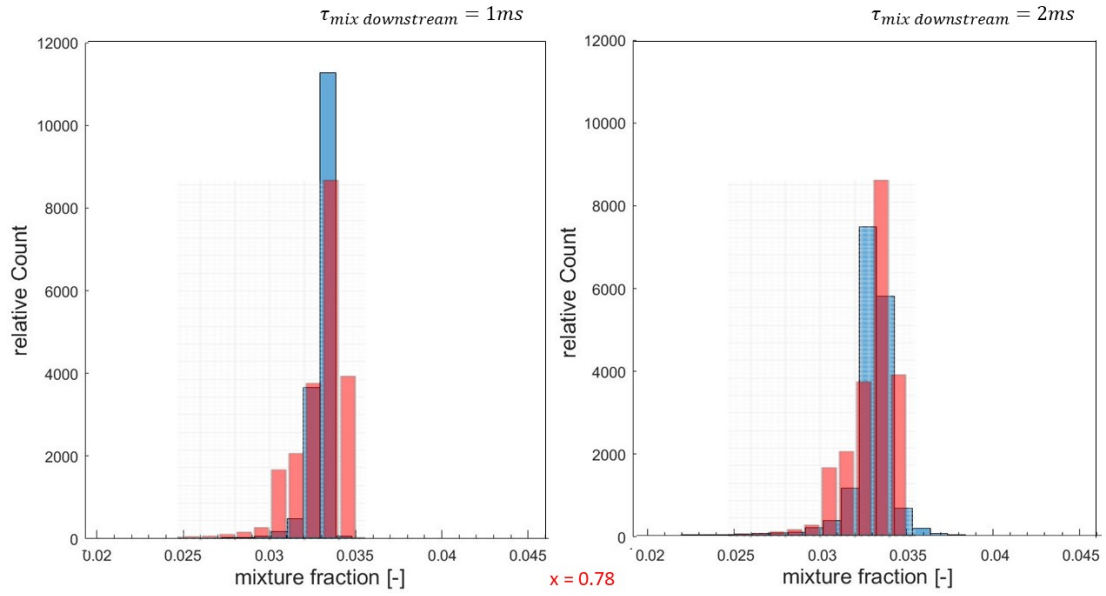

Figure 4.14: Mixture fraction histograms comparison at $x = 0.78$, CFD - red and GeneAC - blue. Left plot: $\tau_{mix,downstream} = 1ms$, right plot: $\tau_{mix,downstream} = 2ms$.

A plot of unmixedness vs. the axial position is presented in Fig. 4.15. The three data series are: CFD, GeneAC with $\tau_{mix,downstream} = 1ms$ and GeneAC with $\tau_{mix,downstream} = 2ms$. The arrows at the bottom of the plot mark the x positions, where air and mixture flows are added.

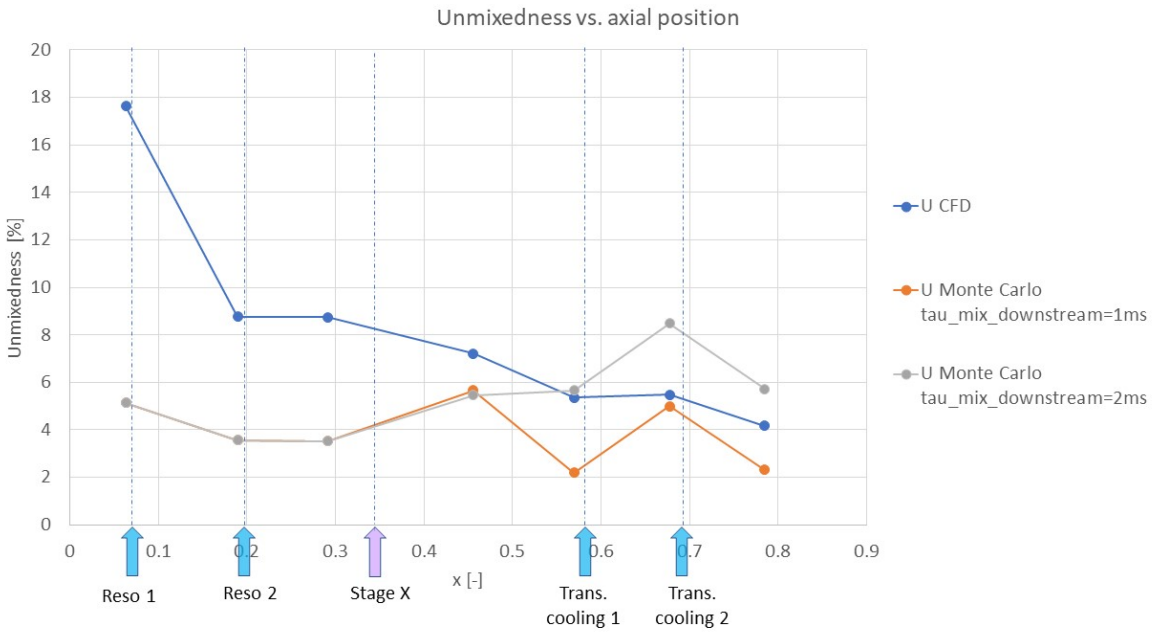

Figure 4.15: Unmixedness vs. axial position for the CFD data, GeneAC with $\tau_{mix,downstream} = 1ms$ and GeneAC with $\tau_{mix,downstream} = 2ms$

As one can see, the GeneAC simulations are strongly under-predicting the unmixedness in the upstream part of the combustor. The difference is the largest in the first cross section - where CFD histogram had a long tail in the lean area (Fig. 4.8). It can be caused by not resolving the resonators in the model - in the simulations both resonators are treated as air flows added at a single point.
In opposition to the GeneAC results, CFD unmixedness is monotonically decreasing throughout the combustor. In the model, addition of the stage X or *Transition cooling* flows visibly increases the U value.
Downstream of the stage X the results are closer to the CFD ones. Still, the CFD unmixedness values lay between the $\tau_{mix,downstream} = 1ms$ and $\tau_{mix,downstream} = 2ms$ - checking intermediate values would be a good idea.

Unfortunately, due to time restrictions, the impact of this new setting on NOx emissions was not evaluated. What is expected is a slight increase in NOx emissions (since unmixedness is larger).

Chapter 5

Summary

5.1 Main Achievements

As a result of this thesis project, GeneAC Monte Carlo tool has undergone numerous improvements. Due to adding useful features, the tool enhanced its accuracy (prescribed pdf) and enabled the user to track mixing downstream of the ignition element (mixture fraction property of the cloud).

After improving the tool itself, a sensitivity analysis of the model was done. It has shown which parameters are particularly important, so require additional attention. Those results were also taken into account when choosing the values for the final model parameters.
After a successful sensitivity analysis, a combustor model was created (in two versions: with and without axial staging).
Using those Monte Carlo tool was successfully validated for $U = 0\%$ cases. As the perfectly mixed case has not shown any major deviations from the general GeneAC results, tool was ready for running the non-zero unmixedness simulations.

Results were compared with experimental data. Their comparison and impact of examined parameters are summed up in subsections 5.1.1-5.1.6.

5.1.1 Impact of the Equivalence Ratio

For $PMP = 5\%$ model returned results, that show exponential dependence of NOx on ϕ. The same behaviour was observable in experiments. Nevertheless those exponential curves were not overlapping - depending on the mechanism NOx emissions were under- or overestimated.

5.1.2 Pressure Impact

The general pressure dependence on NOx was reflected by the model: higher pressure resulted in increased emissions. Nevertheless the power ξ (if assuming the function

$NOx(\phi, p) \approx g(\phi) \cdot p^{\xi}$) of the experiments does not match the one obtained by the model: for both chemical kinetics mechanisms ξ is around 50% smaller.
Also the shape of experimental $\xi(\phi)$ dependence for axial staging does not match the simulation one - all $NOx(\phi)$ curves should be re-evaluated with more data points.

5.1.3 Pilot Fraction Impact

The simulation impact of the PMP on NOx is consistent with physics: stronger pilot results in higher emissions. But except from this basic dependence, the different PMP levels do not show satisfying results - the difference between the NOx (at the same p and ϕ, but different PMP) for experiment is always larger than for the simulation. It means that the Monte Carlo Tool is underestimating the pilot fraction impact on the emissions.

5.1.4 Axial Staging

As in the experiment, the additional stage downstream of the main flames reduced NOx emissions. Even though, the reduction for simulations was smaller, than in the experiments.

5.1.5 NOx Pathway

In GeneAC NOx pathway in the combustor is mostly thermal with additions from N2O and prompt. This situation matches the expectations from the literature - it is mainly the Zeldovich mechanism causing the NOx emissions from the gas turbines' combustors.

5.1.6 Pdf Evaluation

The mixing in the combustor was well resolved in the histograms. The pdfs in the simulation were similar to the ones from CFD. The only difference between them were the width of the distribution - for GeneAC they were too narrow.

5.2 Proposals

GeneAC Monte Carlo tool still requires some work before it can be successfully used by the Siemens Energy combustor designers. The proposals for the future tool developers are presented below.

5.2.1 Flame CFD Investigation

Current model mixing evaluation was carried out basing on histograms in several cross-sections. Future development requires an in-depth CFD investigation in the upstream part of the combustor - the place where unmixedness reaches the highest values. The histograms could be evaluated also for each stage separately. More insight in this area may bring new, improved ideas for modelling the main burners and pilot.

5.2.2 Recirculation

The combustor model used in this thesis project was consisting of only few reactors. Due to this coarse approximation, only the mean flow velocities in each combustion zones were modelled. This way the phenomenon of recirculation was neglected. It is advised to at least do the sensitivity analysis of including separate recirculating flows in the model.

5.2.3 Mixing

The mixing efficiency is not constant in the whole combustor. To be able to set different values in different reaction zones (reactors), mixing time scales should be investigated in CFD in detail.
Another idea for improvement of mixing is making the cooling air flows and stage X more complex than adding the flow in one point - for example by dividing the streams into smaller ones and merging them with the main combustor flow at different x positions.
More complex treatment of the flows added downstream of the flame might lead to more accurate NOx predictions.

5.2.4 Pilot Modelling

As the tool was not able to resolve the PMP impact on NOx, the pilot should be investigated in detail.
More simulations with different pilot settings should be done and compared with the available experimental results.
Also the additional tests focusing on the pilot could be carried out: for example the setting with other stages fuel mass flows set to 0. Also future tool developers should think about changing the way pilot is modelled - by altering the residence/mixing time or using different type of reactor.

5.2.5 Mechanism

The choice of kinetic mechanism has large impact on the results. At the same time, none of two applied mechanisms turned out to be more accurate. Hence choice of the mechanism is still open - NUIG and other available mechanisms should be examined.

Bibliography

[1] Maria Abian, Maria U Alzueta, and Peter Glarborg. Formation of no from n2/o2 mixtures in a flow reactor: toward an accurate prediction of thermal no. *International Journal of Chemical Kinetics*, 47(8):518–532, 2015.

[2] European Environment Agency. European union emission inventory report 1990-2019 under the unece convention of long-range transboundary air pollution (air convention). 2021.

[3] Nelly E Avissar, Christina K Reed, Christopher Cox, Mark W Frampton, and Jacob N Finkelstein. Ozone, but not nitrogen dioxide, exposure decreases glutathione peroxidases in epithelial lining fluid of human lung. *American journal of respiratory and critical care medicine*, 162(4):1342–1347, 2000.

[4] Valter Bellucci, Peter Flohr, Christian Oliver Paschereit, and Fulvio Magni. On the use of helmholtz resonators for damping acoustic pulsations in industrial gas turbines. *J. Eng. Gas Turbines Power*, 126(2):271–275, 2004.

[5] Karin UM Bengtsson, Peter Benz, Rolf Schären, and Christos E Frouzakis. Nyox formation in lean premixed combustion of methane in a high-pressure jet-stirred reactor. In *Symposium (international) on combustion*, volume 27, pages 1393–1399. Elsevier, 1998.

[6] Fernando Biagioli and Felix Güthe. Effect of pressure and fuel–air unmixedness on nox emissions from industrial gas turbine burners. *Combustion and Flame*, 151(1-2):274–288, 2007.

[7] Craig T Bowman. Control of combustion-generated nitrogen oxide emissions: technology driven by regulation. In *Symposium (International) on Combustion*, volume 24, pages 859–878. Elsevier, 1992.

[8] Noeemi A Buczko, Tamaas Varga, Istvan Gy Zsely, and Tamas Turanyi. Formation of no in high-temperature n2/o2/h2o mixtures: re-evaluation of rate coefficients. *Energy & Fuels*, 32(10):10114–10120, 2018.

[9] Sanjay M Correa. A review of nox formation under gas-turbine combustion conditions. *Combustion science and technology*, 87(1-6):329–362, 1993.

[10] Sanjay M Correa. A review of nox formation under gas-turbine combustion conditions. *Combustion science and technology*, 87(1-6):329–362, 1993.

[11] Rane L Curl. Dispersed phase mixing: I. theory and effects in simple reactors. *AIChE journal*, 9(2):175–181, 1963.

[12] Stefan Dederichs, Nikolaos Zarzalis, Peter Habisreuther, Christian Beck, Bernd Prade, and Werner Krebs. Assessment of a gas turbine nox reduction potential based on a spatiotemporal unmixedness parameter. *Journal of engineering for gas turbines and power*, 135(11), 2013.

[13] Merran Evans, Nicholas Hastings, Brian Peacock, and Catherine Forbes. *Statistical distributions*. John Wiley & Sons, 2011.

[14] Charles P Fenimore. Formation of nitric oxide in premixed hydrocarbon flames. In *Symposium (International) on Combustion*, volume 13, pages 373–380. Elsevier, 1971.

[15] MD Fox and Felix Jiri Weinberg. An experimental study of burner-stabilized turbulent flames in premixed reactants. *Proceedings of the Royal Society of London. Series A. Mathematical and Physical Sciences*, 268(1333):222–239, 1962.

[16] Flavio Cesar Cunha Galeazzo, Georg Donnert, Peter Habisreuther, Nikolaos Zarzalis, Richard J Valdes, and Werner Krebs. Measurement and simulation of turbulent mixing in a jet in crossflow. *Journal of Engineering for Gas Turbines and Power*, 133(6), 2011.

[17] Peter Glarborg, James A Miller, and Robert J Kee. Kinetic modeling and sensitivity analysis of nitrogen oxide formation in well-stirred reactors. *Combustion and flame*, 65(2):177–202, 1986.

[18] Siemens Energy GmbH. Sgt-300 in the gas turbines catalogue. https://www.siemens-energy.com/global/en/offerings/power-generation/gas-turbines/sgt-300.html, 2022.

[19] Ponnuthurai Gokulakrishnan and Michael S Klassen. Nox and co formation and control. *Gas turbine emissions*, pages 175–208, 2013.

[20] David M. Golden et. al. Gregory P. Smith. Gri 3.0. http://combustion.berkeley.edu/gri-mech/version30/text30.html#thefiles. Accessed: 2022-03-30.

[21] P Griebel, R Schären, P Siewert, Rolf Bombach, A Inauen, and W Kreutner. Flow field and structure of turbulent high-pressure premixed methane/air flames. 01 2003.

[22] Sharon J Hall, Pamela A Matson, and Philip M Roth. Nox emissions from soil: implications for air quality modeling in agricultural regions. *Annual Review of Energy and the Environment*, 21(1):311–346, 1996.

[23] John B Heywood. Fundamentals of internal combustion engines. *Tata McGraw Hills, New York*, 1988.

[24] Erjiang Hu, Zuohua Huang, Jianjun Zheng, Qianqian Li, and Jiajia He. Numerical study on laminar burning velocity and no formation of premixed methane–hydrogen–air flames. *International journal of hydrogen energy*, 34(15):6545–6557, 2009.

[25] J Janicka, W Kolbe, and W Kollmann. Closure of the transport equation for the probability density funcfion of turbulent scalar fields. 1979.

[26] Witzel B et. al. (Siemens Energy) Krebs W, Schultz A. Advanced combustion system for high efficiency (ace) of the new sgt5/6-9000hl gas turbine. *ASME Turbo Expo 2022*, 2022.

[27] Arnaud Lacarelle, Sebastian Go¨ ke, and Christian O Paschereit. A quantitative link between cold-flow scalar unmixedness and nox emissions in a conical premixed burner. In *Turbo Expo: Power for Land, Sea, and Air*, volume 43970, pages 919–931, 2010.

[28] Chung K Law. *Combustion physics*. Cambridge university press, 2010.

[29] PC Malte and DT Pratt. Measurement of atomic oxygen and nitrogen oxides in jet-stirred combustion. In *Symposium (international) on combustion*, volume 15, pages 1061–1070. Elsevier, 1975.

[30] Norbert Peters. *Turbulent combustion*. Cambridge university press, 2000.

[31] SB Pope. An improved turbulent mixing model. *Combustion Science and Technology*, 28(3-4):131–145, 1982.

[32] Martin Robinius, Alexander Otto, Philipp Heuser, Lara Welder, Chloi Syranidou, David Ryberg, Thomas Grube, Peter Markewitz, R. Peters, and Detlef Stolten. Linking the power and transport sectors—part 1: The principle of sector coupling. *Energies*, 10:956, 07 2017.

[33] A Schlegel, M Streichsbier, R Mongia, and R Dibble. *A Comparison of the Influence of Fuel/Air Unmixedness on NOx Emissions in Lean Premixed, Non-Catalytic and Catalytically Stabilized Combustion*, volume 78699. American Society of Mechanical Engineers, 1997.

[34] Wolfgang Schöpp, Maximilian Posch, Sophia Mylona, and Matti Johansson. Long-term development of acid deposition (1880–2030) in sensitive freshwater regions in europe. *Hydrology and Earth System Sciences*, 7(4):436–446, 2003.

[35] John H Seinfeld. Es&t books: atmospheric chemistry and physics of air pollution. *Environmental science & technology*, 20(9):863–863, 1986.

[36] DA Sullivan. A simple gas turbine combustor no x correlation including the effect of vitiated air. 1977.

[37] George H Tomlinson. Air pollutants and forest decline. *Environmental science & technology*, 17(6):246A–256A, 1983.

[38] Stephen R Turns et al. *Introduction to combustion*, volume 287. McGraw-Hill Companies New York, NY, USA, 1996.

[39] Nevin Uysal and Ralph M Schapira. Effects of ozone on lung function and lung diseases. *Current opinion in pulmonary medicine*, 9(2):144–150, 2003.

[40] Jurgen Warnatz, Ulrich Maas, Robert W Dibble, and J Warnatz. *Combustion*. Springer, 2006.

[41] J Zeldovich. The oxidation of nitrogen in combustion and explosions: Acta. *Physiochem*, 400:401, 1946.

[42] H.s Zhen, C. Leung, and C.s Cheung. A comparison of the heat transfer behaviors of biogas–h2 diffusion and premixed flames. *International Journal of Hydrogen Energy*, 39:1137–1144, 01 2014.

Appendix A

Design of Experiment

Parameters of the test cases selected using DoE and the computed 15% O_2 dry NOx values are presented in the table below (A.1).

Table A.1: Sensitivity analysis results

No.	$\tau_{mix,PSR}$ [ms]	$\tau_{mix,PFR}$ [ms]	U [%]	$\tau_{res,PSR}$ [ms]	Mechanism	NOx (dry, 15% O2)
1	3	3	15	0.15	Turanyi	69.367
2	3	7	5	1.3	Turanyi	32.251
3	1	7	15	0.15	Turanyi	124.588
4	3	3	15	1.3	Turanyi	38.645
5	3	7	5	1.3	Turanyi	32.255
6	3	7	15	0.15	Turanyi	169.971
7	1	7	15	1.3	Turanyi	29.198
8	1	3	15	1.3	Turanyi	25.535
9	1	3	5	1.3	Turanyi	24.605
10	3	3	5	0.15	Turanyi	32.855
11	1	7	5	0.15	Turanyi	43.159
12	1	3	5	0.15	Turanyi	31.607
13	2	5	10	0.7	Turanyi	38.877
14	3	3	15	0.15	GRI3.0	107.338
15	3	7	5	1.3	GRI3.0	72.484
16	1	7	15	0.15	GRI3.0	136.077
17	3	3	15	1.3	GRI3.0	88.551
18	3	7	5	1.3	GRI3.0	73.067
19	3	7	15	0.15	GRI3.0	142.124
20	1	7	15	1.3	GRI3.0	79.421
21	1	3	15	1.3	GRI3.0	69.137
22	1	3	5	1.3	GRI3.0	58.12
23	3	3	5	0.15	GRI3.0	74.162
24	1	7	5	0.15	GRI3.0	81.955
25	1	3	5	0.15	GRI3.0	72.416
26	2	5	10	0.7	GRI3.0	77.622

Appendix B

GeneAC Model

The combustor models with and without the axial stage are presented in the Fig. B.2. They are consisting of following elements (Fig. B.1):

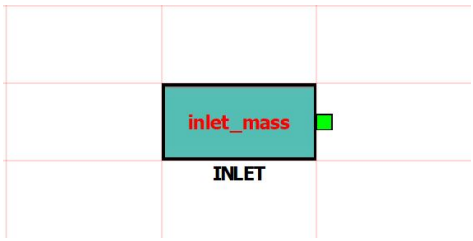

(a) Inlet element

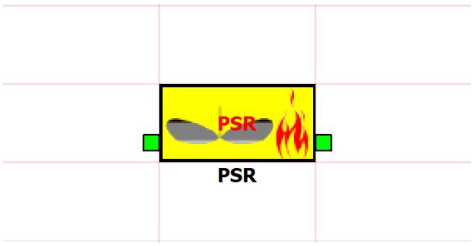

(b) PSR element

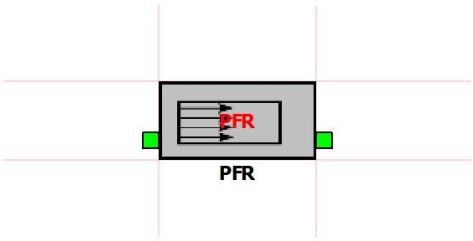

(c) PFR element

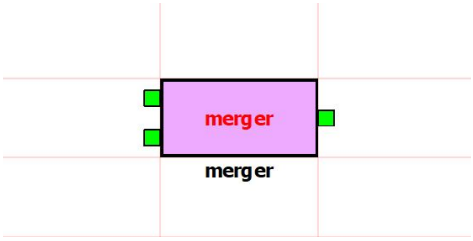

(d) Merger element

Figure B.1: Legend for the models presented in the Fig. B.2

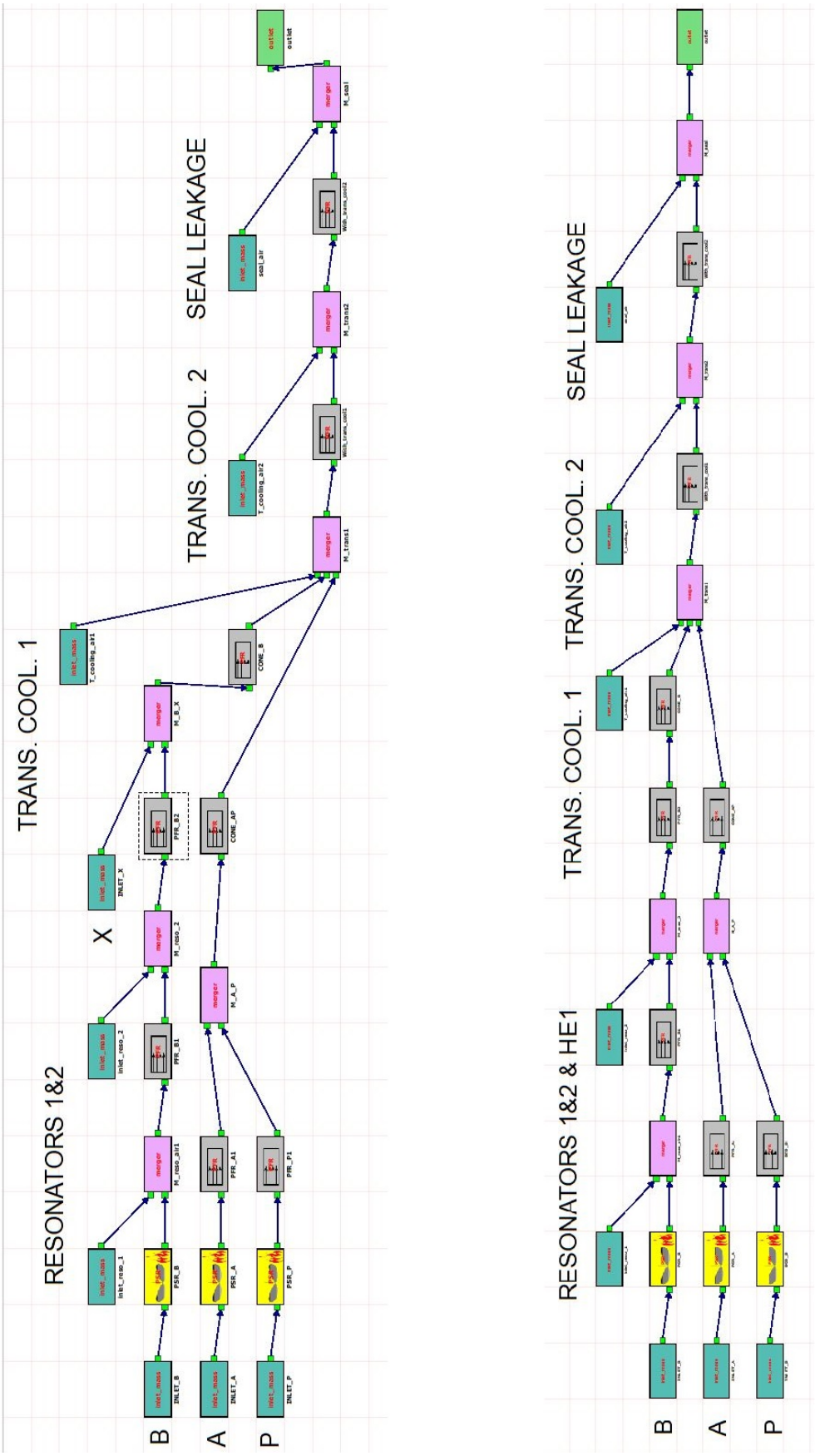

Figure B.2: The model of combustor used in GeneAC (with axial stage X included - on the left side and without including the X stage: on the right side).